Spring 1-1-2013

Enthalpy-Based Models for Ice Sheets and Improving Understanding of Cryo-Hydrologic Warming

Brian Daniel Macpherson
University of Colorado at Boulder, brian.macpherson@colorado.edu

Enthalpy-Based Models for Ice Sheets and Improving Understanding of Cryo-Hydrologic Warming

by

Brian Daniel Macpherson

B.S., Cornell University, 2010

A thesis submitted to the

Faculty of the Graduate School of the

University of Colorado in partial fulfillment

of the requirements for the degree of

Master of Science

Department of Civil, Environmental, and Architectural Engineering

2013

This thesis entitled:
Enthalpy-Based Models for Ice Sheets and Improving Understanding of Cryo-Hydrologic Warming
written by Brian Daniel Macpherson
has been approved for the Department of Civil, Environmental, and Architectural Engineering

Harihar Rajaram

John Crimaldi

Waleed Abdalati

Date

The final copy of this thesis has been examined by the signatories, and we find that both the content and the form meet acceptable presentation standards of scholarly work in the above mentioned discipline.

Macpherson, Brian Daniel (M.S., Civil Engineering)

Enthalpy-Based Models for Ice Sheets and Improving Understanding of Cryo-Hydrologic Warming

Thesis directed by Dr. Harihar Rajaram

There is widespread evidence for a rise in the Equilibrium Line Altitude (ELA) in many areas of the Greenland Ice Sheet. In a recent study (Ettema et al., 2009) West Greenland was found to have experienced a 3.9% increase in area experiencing melt annually. In the wet snow and ablation zones, much of the melt water will enter the englacial hydrologic system via moulins, crevasses and surface fractures (Harper et al., 2012). Of this englacial water, a fraction may persist in the Cryo-Hydrologic System (CHS) (Rennermalm et al., 2012) long enough to refreeze, releasing latent heat and warming the background ice. Because the geometry of the CHS is difficult to constrain, we modeled the small-scale thermodynamics for several end-member scenarios that capture a range of plausible CHS geometries. In particular, we considered crevasses and deeper water bodies subject to one-time water filling, and crevasses that are filled annually and drain via a diffuse drainage system into a fracture network. We found that warming from shallow crevasses is largely driven by 1D horizontal conduction and that the warming is limited by the depth of crevasse penetration. Deep but not fully penetrating englacial water bodies can warm the lower layer of the ice sheet where the increase in the Flow Law Parameter has the greatest impact on ice velocity. The horizontal velocity gradient also caused stretching of deep englacial water bodies, which decreases refreezing time of liquid water at depth. Finally, drainage of crevasses through fracture networks was found to be an efficient mechanism to transport liquid water to depth. The small cross-sectional area, large surface area, and heterogeneity of the fractures provided the fastest and most efficient release of latent heat into the background ice. Based on the modeling results, we propose simple mathematical parameterizations that may be used to represent CHW in large-scale ice sheet models. We also share a new module written for the Community Ice Sheet Model (CISM) that solves the ice sheet thermodynamics using an enthalpy method and replaces a cold ice method module.

Acknowledgements

Thank you Dr. Rajaram for the great advice and support throughout my time at CU-Boulder. Also, thanks to Dr. Crimaldi and Dr. Abdalati for serving on my committee and offering their insight.

Contents

Chapter

Tables

Table

Figures

Figure

Chapter 1

Background

Large-scale glacier and ice sheet models have made significant improvements over recent years in capturing more and more precise details of ice mechanics and thermodynamics. One significant weakness of these models, however, is the interaction between liquid water and ice both within and underneath ice sheet flows. This lack of detail is largely driven by insufficient field and laboratory data that are necessary for a full understanding of the physics behind englacial water creation, movement, and fate. This is starting to be addressed as better non-invasive tools (ice-penetrating RADAR, LIDAR, etc.) are being implemented in the field and englacial water features are being better understood. Even with better observational techniques, the complexity and range of scale of ice and liquid water interaction make it a difficult problem to capture numerically in a large-scale model, and certainly will require simplified parameterizations.

Broadly speaking, there are two kinds of ice-liquid water interactions we are interested in modeling and discuss in this thesis. The first is the interaction between a supraglacial, englacial, or subglacial water-filled body and cold or temperate background ice. These water bodies appear at the surface as the result of meltwater pooling and appear as ponds, streams, crevasses, moulins, fractures, or any combination of these features. These features can drain into englacial water bodies or to the bed of the ice sheet. Also, they can remain stagnant or flow out of the ice sheet into the outlet hydrolgic system. The second ice-liquid water interaction results from the liquid water content of temperate ice. Generally in the range of 0-3% by volume, this liquid water resides in the pore space and at crystal lattices within ice that is at the pressure melting point temperature

(temperate ice).

The numerical treatment of the phase change problem (often called a variation of the Stefan Problem in the literature) is known to be difficult to formulate and solve efficiently due to the large nonlinearity in the specific heat at the phase-change boundary between solid and liquid. Historically, this nonlinearity was dealt with through spatial tracking of the cold-temperate surface (CTS) or simplifying/smoothing techniques at the interface. Recently, however, enthalpy formulations have been presented that recast the advection-conduction equation with enthalpy as the state variable. By doing this, the nonlinearity is moved from the storage term (where the specific heat encapsulates the nonlinearity) to the conduction term [2]. Using enthalpy as a state variable is also convenient in that it captures the energy of both ice and liquid water without losing the ability to diagnostically solve for temperature and liquid water content. While originally developed only to deal with liquid water within temperate ice, we have adapted the formulation to also model water-filled bodies within ice sheets.

Glaciologists and ice sheet modelers have also struggled to establish theoretical predictions of crevasse, moulin, and fracture propagation with and without being water-filled. The complex stress field within an ice sheet is even more difficult to constrain when liquid water is present. If water is able to remain entrapped in these englacial water bodies, refreezing and a transfer of latent heat to the background ice is accomplished. If propagation transfers this liquid water all the way to the bed, the water will be drained subglacially.

In this thesis, I hope to build upon previous work to develop a framework for carefully predicting the thermodynamic and thermomechanical consequences of introducing meltwater into various types of englacial water bodies (crevasses, moulins, and fractures). The geometry and propagation of these englacial water bodies is largely ad-hoc but inspired by field observation and theoretical examinations of supraglacial melt runoff fate. Many end-member scenarios are considered which should provide insight into the range of warming to be expected and its thermomechanical influence. I also examine a Cryo-hydrologic warming (CHW) parameterization incorporated by Thomas Phillips et al. in a Sermeq Avvanarleq flowline model [34] and use the results from

our high-resolution 2D modeling to investigate other potential parameterizations that incorporate CHW as a source term in the advection-conduction equation. It is hoped that a parameterization for CHW will be incorporated in the Community Ice Sheet Model (CISM). CISM is primarily under the administration of the National Center for Atmospheric Research (NCAR) and Los Alamos National Laboratory (LANL),

Finally, I will discuss the development of a new Energy Equation solver for CISM that utilizes the Enthalpy Gradient method described by Aschwanden et al. [2]. I will cover the implementation, validation, and comparison between the Enthalpy Gradient method and the existing Cold Ice method.

1.1 What is Cryo-Hydrologic Warming (CHW)?

CHW is the warming of background ice in a cold ice sheet or glacier due to refreezing of melt water. This melt water can be propagated from the surface into the interior of the ice sheet through englacial conduits such as crevasses, moulins, and fractures. If this liquid water gets halted on its journey downward through a cold ice sheet, it will be given a chance to refreeze, releasing its latent heat into the background ice through conduction and causing a temperature increase. See Figure 1.1 for a schematic of commonly found englacial water bodies. As an example of the potential warming caused by CHW: If 1% of an ice sheet by volume melts and the melt water is uniformly distributed in the ice sheet and allowed to refreeze, a warming of approximately 1.74^oC will result.

1.2 Rising Equilibrium Line Altitude

The presence of englacial water has added significance today as parts of the worlds large ice sheets (Western Greenland in particular) move away from pseudo-steady-state conditions toward a state reflecting warming surface conditions [20]. Surface mass balance models and observations both suggest significant increases in the area of Greenland experiencing melt over the last 20 years [31, 19]. The warmer surface results in the rise of the Equilibrium Line Altitude (ELA), or the

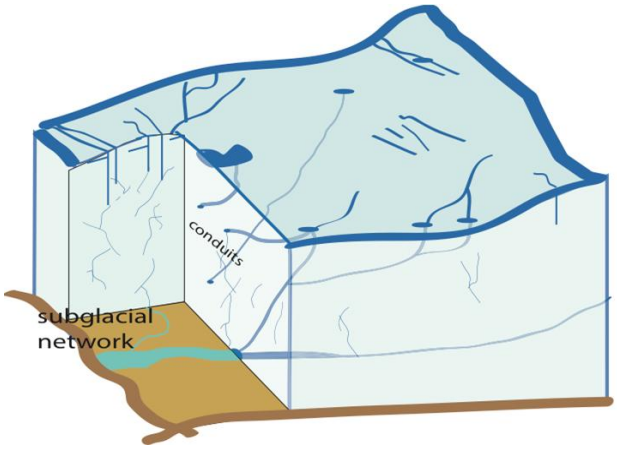

Figure 1.1: Schematic of typical englacial water bodies that can harbor persistent liquid water and cause CHW

altitude at which the ice sheet transitions from an overall ablation zone to overall accumulation zone. Since the ablation zone of an ice sheet has an overall negative mass balance at the surface, this zone of newly-created ablation zone will experience meltwater inputs in the forms of crevasses and moulins not previously seen in the accumulation zone.

As an example, the area of West Greenland experiencing surface melt is increasing at a rate of approximately 3.9 % per year, in response to an estimated $>$ 200 m increase in the equilibrium line altitude between 1990 and 2010 [14]. A more recent assessment [29] suggests a $>$ 500m increase in elevation of the equilibrium line (corresponding to $>$ 40 km inland propagation) and $\approx$ 500m increase in elevation of the maximum inland location of the 0 degree isotherm, a proxy for the dry snow line (corresponding to $>$ 100 km inland propagation). There are several consequences of the upward expansion of the area receiving melt, including a positive albedo feedback [17, 5], which will further increase melt. In the percolation zone, retention of meltwater in the firn serves as a source of near-surface warming reflected in shallow temperature profiles [6, 13]. Recent assessments [21] suggest a large water storage capacity within the firn. At lower elevations in the wet snow and ablation zones, a progressively smaller amount of water storage is available in the firn [24]. However, a significant (but poorly constrained) fraction of meltwater generated on the surface can enter the englacial hydrologic system via moulins, crevasses and surface fractures. The widespread

observations of basal sliding [27] in West Greenland offers indirect evidence that a large amount of meltwater can propagate down to the bed, even in a cold ice sheet. The processes facilitating meltwater penetration to the bed include fracturing, enlargement of moulins, and diffuse drainage through crevasses [9, 30].

1.3 Observed and Theoretical Underpinnings of Persistent Englacial Water

While direct evience of persisent englacial water is elusive, there are numerous theoretical and observational studies that predict its existence or find secondary evidence of its thermal influence. Weertman et al. [41] predicted that given sufficient meltwater input, an isolated crevasse will have a tensile stress below its tip and can extend to the bottom of a glacier. If this meltwater input were to be cut off, a crevasse could presumably extend quite deep without reaching the bed. Van der Veen et al. [40] used a Linear Elastic Fracture Mechanics (LEFM) approach to predict that given sufficient flowrate, crevasses can reach the base of a glacier at a faster rate than refreezing can occur. They found that crevasse propagation downward matched the filling rate in almost all cases. Boon et al. [4] observed a melt and drain event on John Evans Glacier in Arctic Canada where hydrofracturing was hypothesized to drain a supraglacial meltwater network. They observed 8 fracturing and partial draining events that likely refroze before reaching the bed. During the 9th draining event, the supraglacial network completely drained within one hour. The authors hypothesized that this was due to a hydrostatic pressure buildup (as the surface meltwater was at its highest level) and a warming of the cold ice from refreezing of the first 8 fracture events (Cryo-hydrologic warming). Fountain et al. [15] drilled 48 holes into Storglaciären, Sweden, which is a largely temperate alpine glacier of 250m maximum depth. They used a video camera to investigate the englacial water passages they drilled through. They intercepted mostly fractures in the vicinity of refrozen (clear ice) crevasses. Because the glacier was temperate, liquid water persisted in these fractures. Fractures were found to penetrate up to 96% of the ice depth. Catania et al. [8] examined moulins and ice layer stratigraphy near the ELA of Western Greenland using ice penetrating radar. By examing the dip in stratigraphy surrounding a moulin and assuming it was caused by basal

melt from meltwater drainage through the moulin, they estimate the meltwater input required. They found that several supraglacial lakes' worth of water is required to cause the observed melt, indicating that key moulins stay active for several seasons with filling and draining events. Clason et al. [11] modeled supraglacial melt routing to the bed in the Southwest Devon Ice Cap, Nunavut, Canada. Using Van der Veen et al.'s [40] LEFM method, they found that given a meltwater volume, a crevasse is more likely to reach the bed and drain with a 0.5m crevasse width than with a larger width (up to 5m). With a larger width, crevasses are more likely to partially penetrate and remain as stagnant water, allowing refreezing.

It has been shown in several studies that anomalously warm ice profiles can be predicted by accounting for latent heat generated through the refreezing of englacial water bodies [26, 34, 3]. This thermal interaction between englacial water bodies and surrounding cold ice has been called Cryo-Hydrologic Warming (CHW). Ice-penetrating radar was used by Catania et al. [8] to examine ice stratigraphy in the vicinity of moulins in Western Greenland at the Equilibrium Line Altitude. They found that basal melt from supraglacial lake drainage exceeded one draining event, so some moulins must persist for several years. A classic study by Weertman et al. [41] found that isolated water-filled crevasses can extend to the bottom of a glacier given sufficient melt water input. As its depth increased, it would experience refreezing and release latent heat.

Additionally, there are regions of West Greenland that are experiencing increased surface velocities from 10-20 years ago [33]. Without temperature measurements of the ice profile, modeling must be used to test hypotheses regarding the source of increased velocity. The two major hypotheses of the source of velocity increase are increased temperature, which decreases viscosity non-linearly according to Glen's Flow Law, or basal sliding due to increased liquid water at the bed. In this research and the work that precedes it, CHW has been presented as a possible explanation for a rapidly increasing ice temperature, and subsequently higher surface velocity.

1.4 Effect of CHW on Flow Law Parameter and Strain Heat

We are mostly interested in examining the thermomechanical influence of CHW as warming causes an acceleration and increase in strain heat in the ice sheet. According to Glen's Flow Law:

$$\dot{\epsilon} = A\tau^n \tag{1.1}$$

where $\dot{\epsilon}$ is the shear strain rate, τ is shear stress, A is the flow parameter, and n is the creep exponent, usually taken to be 3. The flow parameter, A, follows an Arrhenius relationship for cold ice[13].

$$A_c = A_0 exp\left(-\frac{Q^-}{R\theta}\right) \tag{1.2}$$

where A_0 is a reference value of A, Q_c is the creep activation energy for ice, R is the Universal

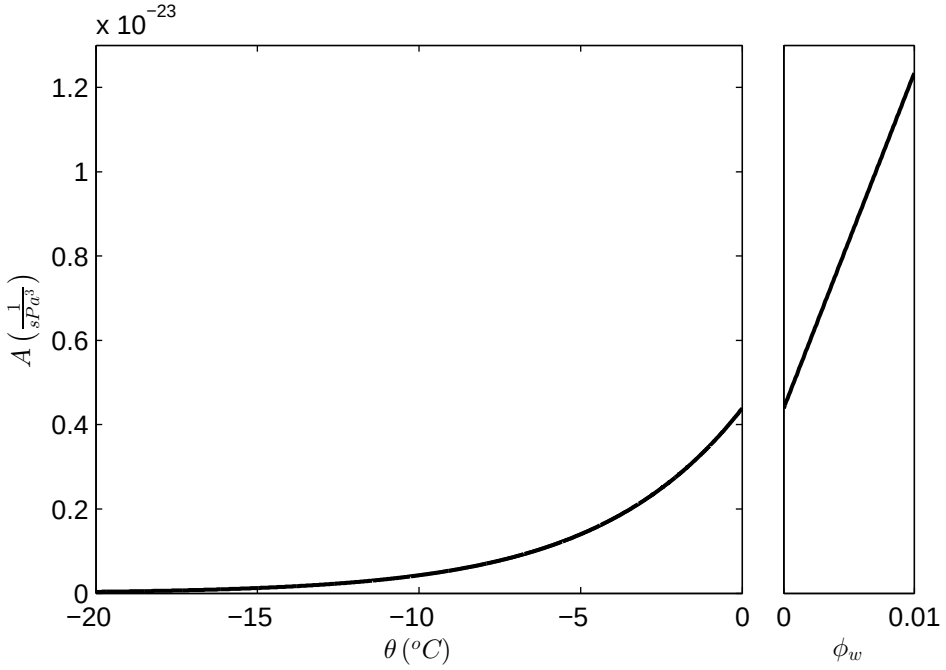

Figure 1.2: Left: Flow Law Parameter A as a function of Temperature in the range experienced in ice sheets. Right: Flow Law Parameter A as a function of Liquid Water Fraction between 0 and 1%, the range typically supported by temperate ice.

Gas Constant, and θ is temperature. For temperate ice [18]:

$$A_t = A_c\left(\theta_{PMP}\right)\left(1 + 181.25\phi_w\right) \tag{1.3}$$

where ϕ_w is the liquid water fraction, θ_{PMP} is the pressure melting point temperature and $A_c\left(\theta_{PMP}\right)$ is Equation 1.2 at $\theta = \theta_{PMP}$. See Figure 1.2.

The flow law parameter A can be understood to be the inverse of viscosity, so warmer and wetter ice result in a higher flow law parameter A and less viscous ice. From Glen's Flow Law, the horizontal velocity gradient of an ice sheet can be derived assuming simple shear [23]. This is referred to as the Shallow Ice Approximation. We can define strain rate in terms of velocity gradient:

$$\dot{\epsilon} = \frac{1}{2}\left(\frac{\partial u}{\partial z} + \frac{\partial w}{\partial x}\right) \tag{1.4}$$

where u and w are the horizontal and vertical velocity, respectively. In simple shear, $\frac{\partial w}{\partial x} = 0$, so

$$\frac{\partial u}{\partial z} = 2A\tau_{zx}^{n} \tag{1.5}$$

Assuming that the surface of the ice sheet has a small slope, we can balance the weight of the ice with a shear stress to derive:

$$\tau_{zx} = \rho g h \sin\alpha_{slope} \approx \rho g h \alpha_{slope} \tag{1.6}$$

where ρ is the ice density, g is gravitational acceleration, h is the height of the ice sheet, and α_{slope} is the surface slope.

$$\frac{\partial u}{\partial z} = 2A\left(\theta\right)\left(\rho g \alpha_{slope}\right)^{n}\left(z_s - z\right)^{n} \tag{1.7}$$

where $z_s - z$ is the depth from the surface. See Figure 1.3 for a typical velocity profile resulting from the integration of Equation 1.7 with a no-slip basal boundary condition. This shows that the horizontal velocity gradient is proportional to the Flow Law Parameter A. We also note from Figure 1.3 that velocity gradient is hightest toward the bottom of the ice sheet due to the $\left(z_s - z\right)^{n}$ term. This means that for warming to have the largest influence on the velocity of an ice sheet, it must occur toward the bottom of the ice sheet.

Additionally, the shear strain rate in the ice sheet is controlled by the flow law parameter A. We can find the strain heat dissipation, Q, from Glen's Flow Law:

$$Q = \dot{\epsilon}\tau = A\tau^{n+1} \tag{1.8}$$

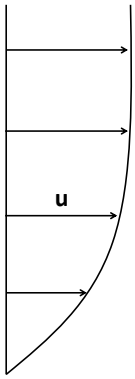

Figure 1.3: A typical ice sheet velocity profile assuming no basal sliding

$$Q = A(\theta)(\rho g \alpha_{slope})^{n+1}(z_s - z)^{n+1} \tag{1.9}$$

Again, we see that strain heat dissipation is proportional to the flow law parameter A.

1.5 Incorporation of Liquid Water in Continental Scale Ice Sheet Models and the Thermomechanical Influence of Warming

Traditional ice sheet modeling would reflect a warming of the surface boundary condition through an increased Type-1 temperature boundary and decreased surface mass balance, which would affect the velocity field of the ice sheet. The time-scale of conduction through a change in the surface boundary temperature is a function of the thermal conductivity of ice. For an ice sheet that is 500 to 1000 m thick, it would take hundreds to thousands of years for this surface warming to be felt throughout the ice sheet. A decrease in the surface mass balance would cause the vertical velocity under the warmed area to change from downward to an upward velocity, further inhibiting a thermal response at depth within the ice sheet. It has been observed in Phillips et al. [34, 33] that there are other feedback mechanisms other than the upper surface boundary that can contribute to the rapid change in ice sheet dynamics and thermodynamics. Developments in the field of ice - liquid water interactions will shed light on this and the inclusion of these interactions in large-scale models will result in more accurate and robust forecasting in Global Climate Models as warming is expected to increase in the 21st century.

1.6 Previous CHW Parameterization

Previous work done by Phillips et al. [34, 33] incorporated the warming effect of cryo-hydrologic warming into an ice-sheet model through a dual-column model of background ice and the cryo-hydrologic system (CHS). A linear exchange term appeared in both the advection-conduction equation modeling the thermodynamics of the background ice and a conduction equation modeling the cryo-hydrologic system. A factor of $\frac{1}{R^2}$ appeared in front of the linear exchange term, with R = half-spacing of cryo-hydrologic systems, to signify a representative spacing between cryo-hydrologic systems. The two equations are solved either iteratively or in sequence to evolve the ice sheet in time. The advection-conduction equation for the background ice is described by equation 1.10.

$$\rho_i C_i \frac{\partial \theta_i}{\partial t} + \rho_i C_i u \frac{\partial \theta_i}{\partial x} + \rho_i C_i w \frac{\partial \theta_i}{\partial z} - \kappa_i \frac{\partial^2 \theta_i}{\partial z^2} = Q + \frac{\kappa_i}{R^2} \left(\theta_{CHS} - \theta_i\right) \tag{1.10}$$

where ρ_i is the ice density, C_i is the ice specific heat, t is time, κ_i is the ice conductivity, Q is strain heat, θ_i is ice temperature, and θ_{CHS} is the cryo-hydrologic system temperature. The cryo-hydrologic system thermodynamics in the winter are described by equation 1.11

$$\frac{\partial \overline{\rho H}_{CHS}}{\partial t} - \frac{\partial}{\partial z}\left(\kappa_{CHS} \frac{\partial \theta_{CHS}}{\partial z}\right) = -\frac{k_i}{R^2} \left(\theta_{CHS} - \theta_{ice}\right) \tag{1.11}$$

where $\overline{\rho H}$ is specific enthalpy and κ_{CHS} is the CHS conductivity. The cryo-hydrologic system thermodynamics in the melt season are described by equation 1.12:

$$\theta_{CHS} = \theta_{PMP} \tag{1.12}$$

1.7 Goals of High-Resolution CHS Modeling

The goal of high-resolution modeling of CHW is to better understand the fundamental physics of the process and to determine what patterns and parameters become important in a large-scale sense. We hope to do this by first developing a modeling framework that tracks specific enthalpy of the cryo-hydrologic system as advection and conduction evolve the system. With a suite of end-member modeling scenarios, we also hope to put bounds on the potential thermodynamic and thermomechanical influence of CHW. While strictly realistic initial introductions of persistent englacial

water, dynamic processes of draining and refilling, and fracture propagation will remain simplified, we expect the results to still glean valuable insight into the fundamental processes. Finally, we hope apply the knowledge gained from this modeling to create alternative parameterizations for large-scale ice sheet models that capture the influence of CHW in a simple, yet physically-justified manner.

Chapter 2

Vertical Column Models

Enthalpy methods are becoming a more widely-adopted way of solving the advection-conduction equation in modeling situations where polythermal ice is encountered. There is a distinct advantage to modeling ice thermomechanics with enthalpy as a state variable instead of temperature for the reason that both temperature and liquid water fraction of ice are functions of enthalpy. In other words, if the enthalpy of the system is known, so are the temperature and liquid water fraction. More details of enthalpy methods will be presented later.

In this section, we consider thermal modeling of vertical columns. In continental-scale ice sheet models or flowline models, thermo-mechanical coupling is typically done with an operator-splitting technique where vertical and horizontal energy transport are considered separately. By creating a transient modeling scenario where initially there is a cold ice profile, then polythermal ice conditions are encountered (temperate ice at the bed and cold ice above) we can compare three different methods for solving the advection-conduction equation in a 1D vertical column (Temperature-Based CTS Tracking, Apparent Heat Capacity Approach, and the Enthalpy Gradient Method). Only the thermodynamics of the system are considered here - there is no thermomechanical coupling in this section.

The same transient test case was run for each modeling approach. The column had a height of 800m and had an initial temperature of -5^{o}C. There were two source terms of heat in the test case - frictional strain heat and a horizontal advection parameterization. The strain heat term produces warmth primarily at the bed of the column and is responsible for warming the bed to

temperate conditions over time. Strain heat can be derived from Glen's Flow Law which relates stress and strain in glacier flow. See Equations 1.8 and 1.9. This value of Q was multiplied by 100 so that a temperate basal layer was encountered.

2.1 CTS Tracking

The tradational way of modeling ice thermodynamics is with the temperature-based advection-conduction equation:

$$\frac{\partial \theta}{\partial t} + u\frac{\partial \theta}{\partial x} + w\frac{\partial \theta}{\partial z} - \frac{\partial}{\partial z}\left(\alpha \frac{\partial \theta}{\partial z}\right) = \frac{Q}{\rho\, C} \tag{2.1}$$

where $\alpha = \frac{\kappa}{\rho C}$ is the diffusivity of ice, κ is the conductivity of ice, and C is the specific heat. $u\frac{\partial \theta}{\partial t}$ can be approximated by $u(z)\alpha_{slope}\lambda$ where α_{slope} is the surface slope and λ is the lapse rate. At the cold-temperate surface interface, there is a flux balance of heat:

$$-\kappa \left.\frac{\partial \theta}{\partial z}\right|_{+} = -\kappa \left.\frac{\partial \theta}{\partial z}\right|_{-} + \rho_w \phi_w L \tag{2.2}$$

where ϕ_w is the liquid water fraction and L is the latent heat of fusion. In order to calculate this flux balance, an assumed liquid water fraction of the temperate ice must be assumed. It has been observed that 1% liquid water fraction is reasonable in temperate ice before draining starts to occur. We can balance the heat fluxes above and below the CTS:

$$\left.\frac{\partial \theta}{\partial z}\right|_{+} = \left.\frac{\partial \theta}{\partial z}\right|_{-} + \frac{\rho_w \phi_w L}{\kappa} \tag{2.3}$$

and since (-), or the ice below the CTS, is temperate ice,

$$\left.\frac{\partial \theta}{\partial z}\right|_{-} = \frac{\partial \theta_{PMP}}{\partial z} \tag{2.4}$$

$$\left.\frac{\partial \theta}{\partial z}\right|_{+} = 6.7x10^{-4}\frac{^oC}{m} - \frac{\rho_w \phi_w L}{\kappa_w} \tag{2.5}$$

We also know that $\theta|_{+} = \theta_{PMP}$, so both basal boundary conditions for the cold, upper layer of ice must simultaneously be satisfied. The temperate ice below the CTS is at PMP. In an iterative process, the CTS is moved and a temperature profile is solved for the cold, upper layer of ice using the Type-2 boundary condition at the CTS. The iteration is completed until the Type-1 boundary layer is also satisfied within some tolerance.

2.2 Enthalpy Gradient Method

We can transform the advection-conduction equation from a temperature-based equation into an enthalpy-based equation by:

$$\overline{\rho H} = (1-\phi_w)\,\rho_i C_i\,(\theta-\theta_0) + \phi_w \rho_w\,[C_i\,(\theta_{PMP}-\theta_0) + C_w\,(\theta-\theta_{PMP}) + L] \tag{2.6}$$

where $\overline{\rho H}$ is specific enthalpy and θ_0 is an arbitrary reference temperature, which is simply $\overline{\rho H} = \rho_i C_i \theta$ for cold ice and $\theta_0 = 0^o C$. So now the advection-conduction equation (for cold ice) is:

$$\frac{\partial \overline{\rho H}}{\partial t} + u\frac{\partial \overline{\rho H}}{\partial x} + w\frac{\partial \overline{\rho H}}{\partial z} - \frac{\partial}{\partial z}\left(\alpha \frac{\partial \overline{\rho H}}{\partial z}\right) = Q \tag{2.7}$$

where $\alpha = \frac{\kappa}{\rho\, C}$ is the diffusivity of ice, u and w are horizontal and vertical velocity, respectively, and Q is frictional strain heat.

When dealing with temperate or polythermal conditions, a different formulation is needed for the conductive energy flux term. In the cold case, conductive flux is governed by Fouriers Law of Heat Transfer and is simply a sensible heat flux. In the temperate ice case, the conductive heat flux is the sum of a sensible and latent heat flux, which can both be expressed as diffusive processes. The sensible heat flux, $\kappa_i \frac{\partial \theta_{PMP}}{\partial z}$ arises from a temperature gradient due to pressure-induced changes in θ_{PMP} with depth. Assuming hydrostatic conditions and the Clausius-Clapyron relation, however, means that θ_{PMP} varies linearly with depth, so $\frac{\partial \theta_{PMP}}{\partial z} = -\beta$, a constant. In a 1D column model, this results in $\frac{\partial}{\partial z}(-\beta) = 0$, so the term can be neglected. In a 2D model, non-linear spatial variations in θ_{PMP} can exist in horizontally neighboring nodes with different ice depths, resulting in non-zero sensible heat exchange. Aschwanden et al. [2] showed that even with relatively steep surface slope, this term can reasonably be neglected. The latent heat flux results from diffusion of liquid water within temperate ice. The latent heat flux is proportional to the liquid water content, so is $\kappa_0 \frac{\partial \phi_w}{\partial z}$, where κ_0 is a small unknown diffusion-like parameter. We can say that liquid water fraction is linearly related to enthalpy by:

$$\phi_w = HL^{-1} \tag{2.8}$$

where H is enthalpy when $\theta = \theta_{PMP}$ as we will see later. This allows us to define $\alpha_0 = \kappa_0 L^{-1}$ which is a small diffusivity and keep $\overline{\rho H}$ as our state variable. This diffusion of liquid water within ice is poorly understood, but has been observed to resemble a Fick-type diffusion. The conductive heat flux is shown in Equation 2.9 and the new Advection-Conduction equation is written out in Equation 2.10.

$$J_{conduction} = \begin{cases} \alpha_i \frac{\partial \overline{\rho H}}{\partial z} & \overline{\rho H} < \overline{\rho H}_{PMP} \\ \kappa_i \frac{\partial \theta_{PMP}}{\partial z} + \alpha_0 \frac{\partial \overline{\rho H}}{\partial z} & \overline{\rho H} \geq \overline{\rho H}_{PMP} \end{cases} \tag{2.9}$$

$$\frac{\partial \overline{\rho H}}{\partial t} + u\frac{\partial \overline{\rho H}}{\partial x} + w\frac{\partial \overline{\rho H}}{\partial z} - \frac{\partial}{\partial z}\left(J_{conduction}\right) = Q \tag{2.10}$$

Once $\overline{\rho H}$ is calculated in each time-step, temperature and liquid water fraction can both be calculated as they are both functions only of enthalpy.

$$\theta = \begin{cases} \frac{\overline{\rho H}}{\rho_i C_i} & \overline{\rho H} < \overline{\rho H}_{PMP} \\ \theta_{PMP} & \overline{\rho H} \geq \overline{\rho H}_{PMP} \end{cases} \tag{2.11}$$

$$\phi_w = \begin{cases} 0 & \overline{\rho H} < \overline{\rho H}_{PMP} \\ \frac{\left(\overline{\rho H} - \overline{\rho H}_{PMP}\right)}{(\rho_w - \rho_i) C_i \theta_{PMP} \rho_w L} & \overline{\rho H} \geq \overline{\rho H}_{PMP} \end{cases} \tag{2.12}$$

where $\overline{\rho H}_{PMP}$ is the specific enthalpy of ice at $\theta = \theta_{PMP}$ and no liquid water fraction.

2.3 Apparent Heat Capacity Approach

The standard advection-conduction equation (with horizontal advection parameterization):

$$\frac{\partial \overline{\rho H}}{\partial t} + w\frac{\partial \overline{\rho H}}{\partial z} - \frac{\partial}{\partial z}\left(\kappa_i \frac{\partial \theta}{\partial z}\right) = Q - u\left(z\right)\rho C \alpha \lambda \tag{2.13}$$

can be transformed with the chain rule:

$$\frac{\partial \overline{\rho H}}{\partial \theta}\frac{\partial \theta}{\partial t} + w\frac{\partial \overline{\rho H}}{\partial \theta}\frac{\partial \theta}{\partial z} - \frac{\partial}{\partial z}\left(\kappa_i \frac{\partial \theta}{\partial z}\right) = Q - u\left(z\right)\rho C \alpha \lambda \tag{2.14}$$

$\frac{\partial \overline{\rho H}}{\partial \theta} = \rho C$ where C is the heat capacity. When dealing with temperate and polythermal ice, we can define C_a and κ_a as apparent heat capacity and apparent conductivity in order to deal with

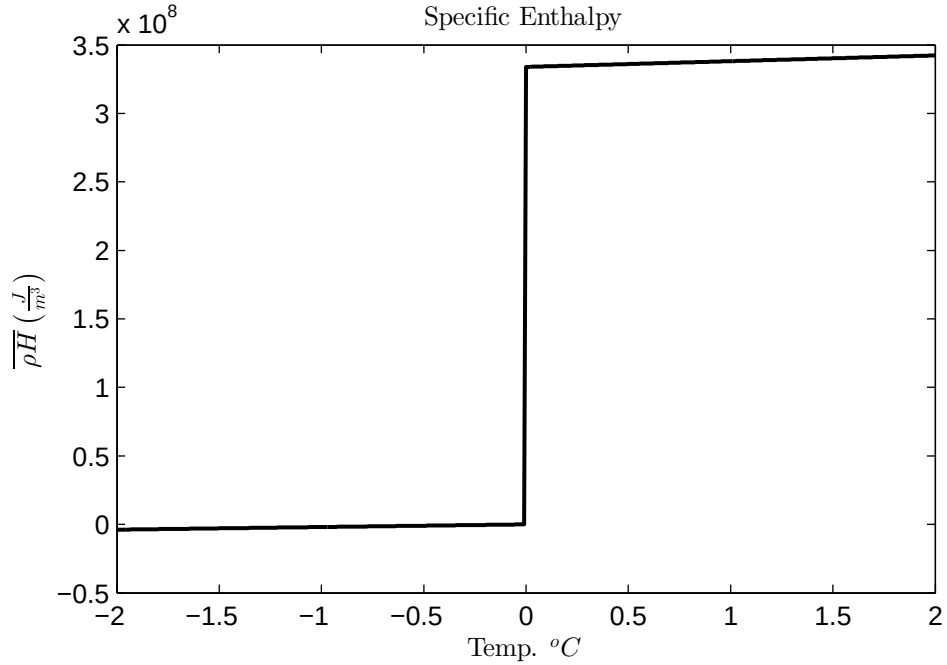

Figure 2.1: Specific Enthalpy as a function of temperature

the Stefan Problem at the cold-temperate interface [28]. When we look at a plot of enthalpy vs. temperature, we see that there is a jump in enthalpy at the pressure-melting point (Figure 2.1).

Since $\frac{\partial H}{\partial \theta} = C$, there is an infinite heat capacity at θ_{PMP}. Instead of causing a rise in temperature, heat flux causes a phase change (melt). Since an infinite heat capacity would imply that no heat is transferred between cold and temperate ice, we can say that instead of phase change happening at exactly θ_{PMP}, it happens over a small $\Delta\theta$ such that

$$\int_{\frac{-\Delta\theta}{2}}^{\frac{\Delta\theta}{2}} C_a(\theta)\, d\theta = L \tag{2.15}$$

This allows enthalpy to increase by L over the range $\frac{-\Delta\theta}{2}$ to $\frac{\Delta\theta}{2}$, but prevents the heat capacity from becoming infinite. Instead, $\rho C_a = \frac{\rho L}{\Delta\theta}$ in the range $\frac{-\Delta\theta}{2}$ to $\frac{\Delta\theta}{2}$. This is shown in Figure 2.2.

$$C_a = \begin{cases} C_i & \theta < \theta_{PMP} - \frac{\Delta\theta}{2} \\ \frac{L}{\Delta\theta} & \theta_{PMP} - \frac{\Delta\theta}{2} \leq \theta \leq \theta_{PMP} + \frac{\Delta\theta}{2} \\ C_w & \theta > \theta_{PMP} + \frac{\Delta\theta}{2} \end{cases} \tag{2.16}$$

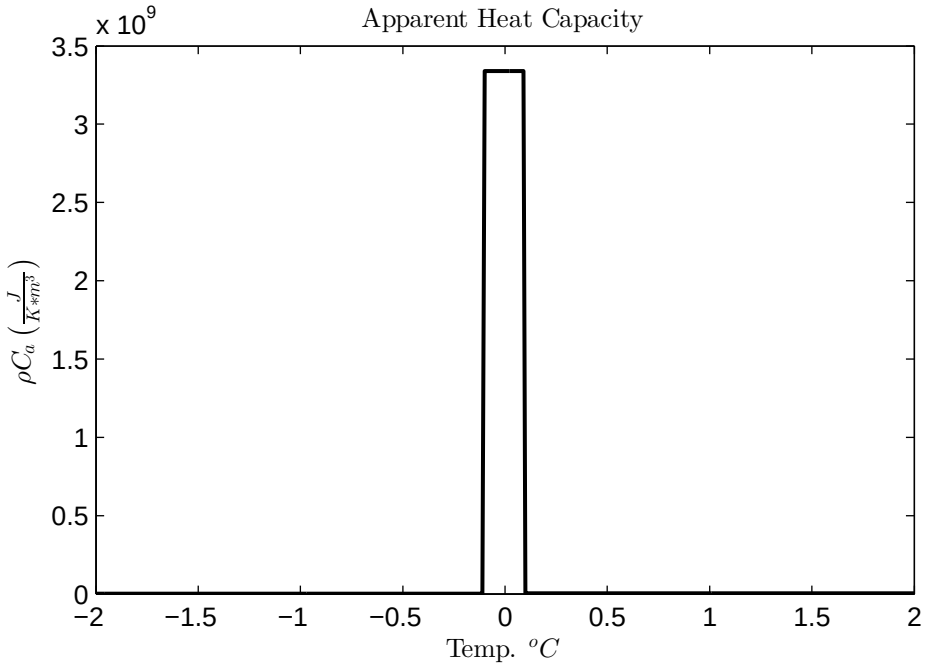

Figure 2.2: Apparent Heat Capacity as a function of temperature for $\Delta\theta = 0.1^oC$

We also define κ_a to vary linearly between κ_i and κ_w in the region $\frac{-\Delta\theta}{2}$ to $\frac{\Delta\theta}{2}$ in order to reflect that water content of the ice increases linearly from 0 to 1 from $\frac{-\Delta\theta}{2}$ to $\frac{\Delta\theta}{2}$. This is shown in Figure 2.3.

$$\kappa_a = \begin{cases} \kappa_i & \theta < \theta_{PMP} - \frac{\Delta\theta}{2} \\ \kappa_i + \frac{\kappa_i - \kappa_w}{\Delta\theta}\left[\theta - \left(\theta_{PMP} - \frac{\Delta\theta}{2}\right)\right] & \theta_{PMP} - \frac{\Delta\theta}{2} \leq \theta \leq \theta_{PMP} + \frac{\Delta\theta}{2} \\ \kappa_w & \theta > \theta_{PMP} + \frac{\Delta\theta}{2} \end{cases} \tag{2.17}$$

2.4 Comparison of Column Models

A comparison of the three methods for dealing with temperate ice was conducted in order to find pros and cons to each method and to see differences in the temperature profiles obtained. Once vetted, any of these three methods can be adapted to a flowline model. Only the enthalpy method and apparent heat capacity method are easily adaptable to the 2D crevasse model where the advection-conduction equation is applied to an enthalpy field consisting of pure liquid water and ice with a moving boundary (Stefan Problem).

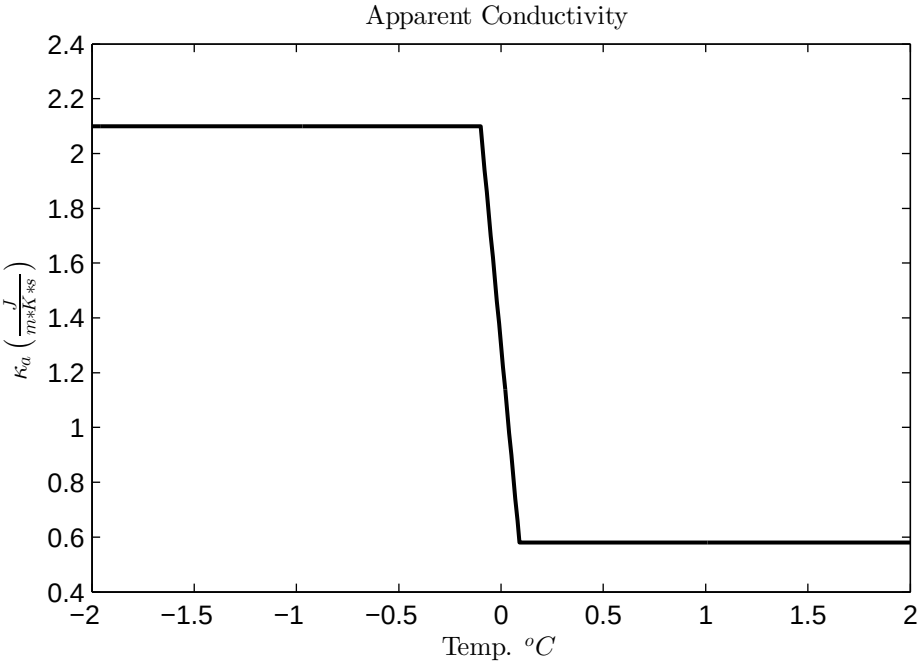

Figure 2.3: Apparent Conductivity as a function of temperature for $\Delta\theta = 0.1^oC$

In order to encounter temperate conditions, a test-case was used that included artificially high strain heating as a source term (100 times greater than would normally be derived from a Glens Flow Law velocity profile). This allowed us to examine how each model handled the transition from cold to temperate conditions. The test case involved a Type-1 boundary condition at the surface and a changing boundary condition at the base depending on whether the ice is cold or temperate and the method used. The column had a depth of 800m with $\Delta z = 1m$. A lapse rate of $\lambda = 0.0055K/m$ and surface slope of $\alpha_{slope} = 0.0075$ were used for the horizontal advection term. $u\frac{\partial\theta}{\partial x}$ can be approximated by $u\left(z\right)\alpha_{slope}\lambda$. To derive the velocity profiles, the Shallow Ice Approximation was used for the horizontal velocity and an ablation rate was used to create a linear vertical velocity profile in Equation 2.18.

$$u(z) = u_b + 2A\left(\rho g \alpha_{slope}\right)^{\frac{3}{4}}\left(H^4\left(H-z\right)^4\right) \tag{2.18}$$

where u_b is the basal horizontal velocity. We used values of $u_b = 0$ and $A = 3x10^{-24}$ [13]. The

vertical velocity profile is expressed in Equation 2.19

$$w(z) = b\left(\frac{z}{H}\right) + b_m\left(1 - \frac{z}{H}\right) \tag{2.19}$$

where $b = 0.25m/a$ is the ablation rate and $b_m = 0$ is the basal melt rate. The strain rate was also developed from the Shallow Ice Approximation velocity profile:

$$Q = 2A\left(\rho g \alpha_{slope}\left(H - z\right)^4\right) \tag{2.20}$$

As mentioned, a strain rate of 100*Q was used to create temperate conditions at the bottom of each column profile. The transient model was run at a 30 day time-step for 1000 years to reach a quasi-steady state. The surface boundary condition was $\theta_{surface} = -5^oC$ and the initial temperature at all depths was $\theta_0 = -5^oC$.

We see in Figure 2.4 that the three methods all produce temperate bed conditions for roughly the bottom $70m$ of the column profile. The apparent heat capacity method produced water content in the ice that varied almost linearly from 0 at the cold-temperate interface to about 2% at the bed. The enthalpy method also produced a linear profile of water content that varied from 0 at the cold-temperate interface to 1.4% at the bed. Finally, the CTS tracking method produced a similar temperature profile as the preceding two methods with a temperate base of $78m$. Since the CTS heat-flux is a function of water content, assumed water content must be used, meaning that the temperate ice is uniformly assumed to be 1% liquid water fraction.

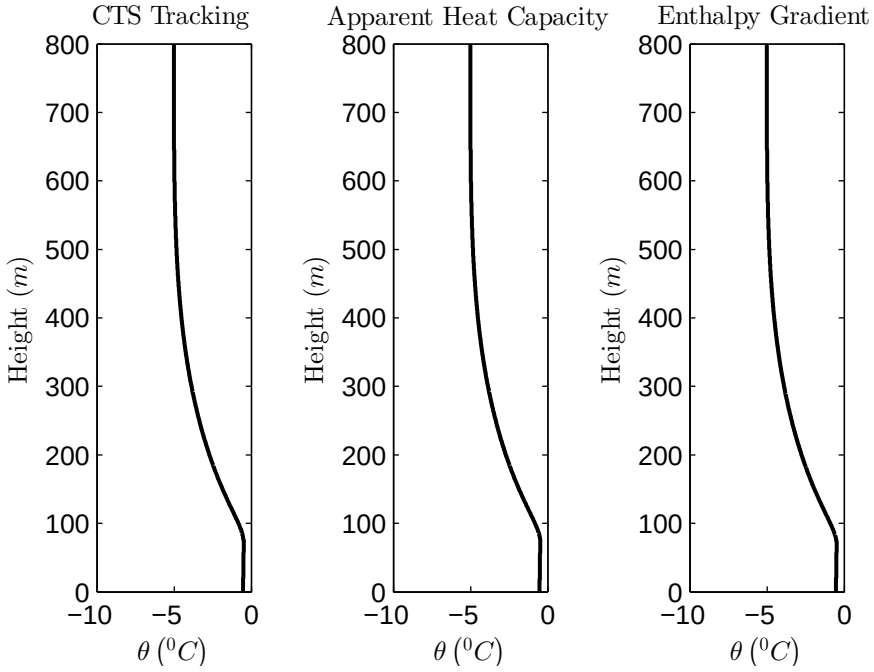

(a) Temperature Comparison

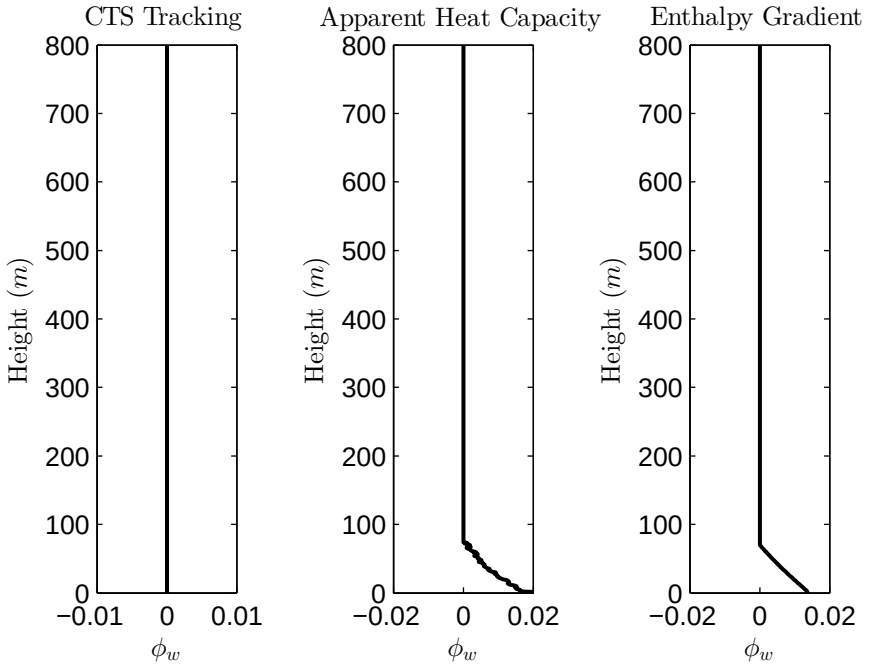

(b) Liquid Water Fraction Comparison

Figure 2.4: Column Model Comparison

Chapter 3

Crevasse Refreezing Rate

One of the major uncertainties with the enthalpy gradient method is the value to assign to the temperate diffusivity, α_0 (see Section 2.2). For small values of liquid water fraction, the gradient between the enthalpy of cold and temperate ice is small, and the rate of heat transfer from temperate ice to cold ice is insensitive to the value of α_0 [2]. In a cryo-hydrologic system, however, there is initially liquid water (treated as temperate ice with 100% liquid water fraction) in direct contact with cold ice. In these neighboring nodes, there is a large jump in enthalpy (by at least the latent heat of fusion). The rate that heat is transferred from the liquid water to the surrounding cold ice (and hence refreezing of the liquid water) is heavily dependent on α_0. As the value of α_0 is not well constrained in the literature, tests were performed to match crevasse refreezing rates generated numerically with the Enthalpy Gradient Method using different values of α_0 to an approximate analytical solution of the Stefan problem, the Apparent Heat Capacity Method, and an Ice-Water Interface solution of the enthalpy formulation. There are also uncertain parameters that affect refreezing rate in the Apparent Heat Capacity solution, so sensitivities to those parameters will also be examined in this section.

The same 1D numerical test case was examined using the Enthalpy Gradient Method, Apparent Heat Capacity Method, and Ice-Water Interface solution. This 1D test case was chosen to match the assumptions of the analytical Stefan solution, including the initial conditions and boundary conditions. The Type-1 boundary far from the CTS is $\theta = \theta_0$, where θ_0 is some cold ice temperature. Since the Stefan solution transitions from θ_{PMP} to θ_0 with an error function, it is

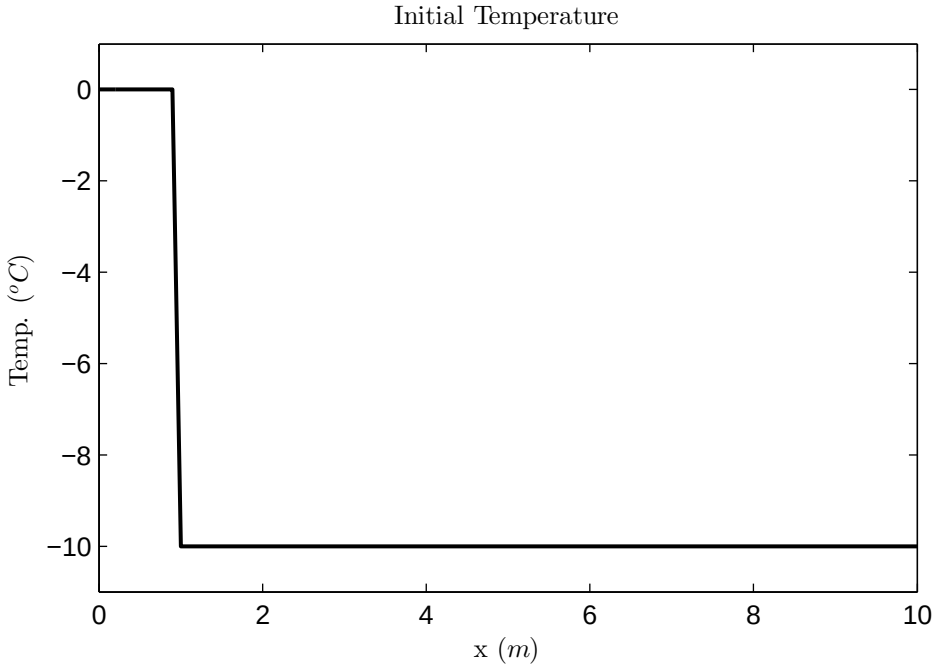

Figure 3.1: Initial Temperature profile for refreezing problem. The ice domain extends to x=60m.

important that the numerical solutions have a large enough domain such that the warming from the liquid water never "feels" the cold boundary at θ_0 as the solution would then deviate from an error function. The test case initially had 1m of liquid water on the left of the domain and 59m of cold ice at $\theta_0 = -10^oC$ on the right of the domain. 59m is a large enough domain to be approximated as semi-infinite. See Figure 3.1 for the initial conditions of the problem. The left boundary condition was a no-flux boundary such that

$$\frac{\partial \theta}{\partial x} = 0 \text{ at x=0m} \tag{3.1}$$

The right boundary condition is a Type-1 held at:

$$\theta_0 = -10^oC \text{ at x=L=60m} \tag{3.2}$$

3.1 Apparent Heat Capacity Approach

The Apparent Heat Capacity Approach used here is similar to the approach outlined in Section 2.3, but varies in the way an initial condition is applied. Whereas a temperate bed was

built up from cold initial conditions in the Column Model section, here we are starting with 1m of pure liquid water and 59m of cold ice at $\theta = -10^oC$. This means that the liquid water must start at temperature $\theta_{PMP} + \Delta\theta$ so that $C_a = C_w$ and $\kappa_a = \kappa_w$ as defined in the Column Model section. As refreezing occurs, the temperature of the liquid water drops from $\theta_{PMP} + \Delta\theta$ to θ_{PMP}. Once $\theta < \theta_{PMP}$, the water is considered to be refrozen. The time required to refreeze the water may dependend on $\Delta\theta$, though it is not intuitively clear if there will be any direct relationship. While a larger $\Delta\theta$ means liquid water will have to undergo a larger decrease in temperature in order to refreeze, a larger $\Delta\theta$ also means there will be a smaller Apparent Heat Capacity as $C_a = \frac{L}{\Delta\theta}$ in the region $\theta_{PMP} < \theta < \theta_{PMP} + \Delta\theta$.

3.2 Water-Ice Interface Method

With this method, the initial conditions are applied and an exact numerical treatment of the ice-water interface is examined to calculate a refreezing time. The ice-water interface condition is:

$$-\kappa_w \frac{\partial \theta_w}{\partial x} + \kappa_i \frac{\partial \theta_i}{\partial x} = \pm \rho_w L \frac{\partial X}{\partial t} \tag{3.3}$$

where X is the water-ice interface location. To address the issue of a partial node freezing in a timestep, a variable timestep is used that allows one full node to refreeze per timestep. To accomplish this, the interface condition is rewritten as

$$\frac{\partial X}{\partial t} = \frac{\kappa_i}{\rho_w L} \frac{\partial \theta_i}{\partial x} \tag{3.4}$$

since $\frac{\partial \theta_w}{\partial x} = 0$. Then, to determine the time Δt it takes to refreeze a full node:

$$\Delta t = \frac{\Delta x}{\frac{\partial X}{\partial t}} \tag{3.5}$$

where Δx is the node spacing. With this variable Δt, each timestep consists of moving the interface to the left one full node and solving the cold conduction equation to the right of the interface.

Since the initial condition on the ice side is $\theta_i = -10^oC$, there is initially no temperature gradient to drive the interface freezing condition. Therefore, one small fixed timestep is done where

the ice temperature to the right of the interface is brought to $\theta = 0^oC$ and the cold conduction equation is solved. A small timestep (1 day) is used so that the assumption that no refreezing occurs is valid. After this small timestep, there is a temperature gradient $\frac{\partial \theta_i}{\partial x}$ so that the interface condition can be satisfied.

3.3 Analytical Solution

An approximate analytical solution exists for the refreezing problem as laid out by Lunardini et al. [28]. The original class of problem was first proposed and solved by Stefan in 1891 as it pertained to the freezing of sea ice. It has since been applied to a wide range of heat transfer problems involving a moving phase change boundary. The same method (with different initial conditions) is laid out here.

Initially to the left we have $\theta_w = \theta_{PMP}$ from $x = -1m$ to $x = 0m$. To the right, we have a semi-infinite domain of ice at $\theta_i = \theta_0$. $X(t)$ is the interface location and initially is at $X(0) = 0m$. At $t = 0$, the ice temperature at the interface boundary is brought to $\theta_i = \theta_{PMP}$.

There are two phase change interface conditions that must be satisfied at all times:

$$\theta_i = \theta_{PMP} \text{ at } x = X(t) \tag{3.6}$$

$$-\kappa_i \frac{\partial \theta_i}{\partial x} = -\rho_w L \frac{\partial X(t)}{\partial t} \text{ at } x = X(t) \tag{3.7}$$

Once conduction starts, a heat-transfer similarity solution is applied to the ice temperature:

$$\theta_i = \theta_0 + A\ erfc\left(\frac{x}{2\sqrt{\alpha_i t}}\right) \tag{3.8}$$

Applying the first phase change interface condition:

$$\theta_{PMP} = \theta_0 + A\ erfc\left(\frac{X(t)}{2\sqrt{\alpha_i t}}\right) \tag{3.9}$$

Using a Fourier Series solution we can say:

$$X(t) = -2\gamma\sqrt{\alpha_i t} \tag{3.10}$$

$$\theta_{PMP} = \theta_0 + A\ erfc\,(-\gamma) \tag{3.11}$$

$$A = \frac{\theta_{PMP} - \theta_0}{erfc\left(-\gamma\right)} \tag{3.12}$$

Now going back to our second phase change boundary condition:

$$\frac{\partial \theta_i}{\partial x} = \frac{-A \exp\left(\frac{-x^2}{4\alpha_i t}\right)}{\sqrt{\pi \alpha_i t}} \tag{3.13}$$

$$\frac{\partial X(t)}{\partial t} = \frac{-\gamma\sqrt{\alpha_i}}{\sqrt{t}} \tag{3.14}$$

so at $x = X(t)$

$$\frac{\kappa_i A}{\sqrt{\pi \alpha_i t}} \exp\left(\frac{-X(t)^2}{4\alpha_i t}\right) = -\rho_w L \frac{-\gamma\sqrt{\alpha_i}}{\sqrt{t}} \tag{3.15}$$

$$\frac{\kappa_i \left(\theta_{PMP} - \theta_0\right)}{\sqrt{\pi \alpha_i}\ erfc\left(-\gamma\right)} \exp\left(-\gamma^2\right) = \rho_w L \gamma \sqrt{\alpha_i} \tag{3.16}$$

Moving all the γ terms to the left side, we have:

$$\frac{\exp\left(-\gamma^2\right)}{\gamma\ erfc\left(-\gamma\right)} = \frac{\rho_w L \sqrt{\pi} \alpha_i}{\kappa_i \left(\theta_{PMP} - \theta_0\right)} \tag{3.17}$$

Assuming that γ is small, we can make two simplifying assumptions. First, $erfc\left(-\gamma\right) = 1$ for small γ and $\exp\left(-\gamma^2\right) = 1$ for small γ. This results in:

$$\gamma = \frac{\kappa_i \left(\theta_{PMP} - \theta_0\right)}{\rho_w L \sqrt{\pi} \alpha_i} \tag{3.18}$$

It is important to check that this results in a small γ so that the previous two assumptions hold. In the case where $\theta_{PMP} - \theta_0 = 10^o C$, $\gamma = .033$ using Equation 3.18. Plugging this value back into Equation 3.17 results in 3.6% error, an acceptable value. If $\theta_{PMP} - \theta_0 = 20^o C$ is used, a 7.8% error occurs, so an iterative approach to solving Equation 3.17 is desirable. This value of γ can then be used to solve the location of the phase change boundary as a function of time:

$$X\left(t\right) = -2\gamma\sqrt{\alpha_i t} \tag{3.19}$$

3.4 Enthalpy Gradient Method

The approach used in this section is similar to the column model formulation found in Section 2.2, but with polythermal initial conditions, no strain heat, and no advection. The governing

equation can be found in Equation 3.20 and 3.21

$$\frac{\partial \overline{\rho H}}{\partial t} - \frac{\partial}{\partial x}\left(J_{conduction}\right) = 0 \tag{3.20}$$

$$J_{conduction} = \begin{cases} \alpha_i \frac{\partial \overline{\rho H}}{\partial x} & \overline{\rho H} < \overline{\rho H}_{PMP} \\ \kappa_i \frac{\partial \theta_{PMP}}{\partial x} + \alpha_0 \frac{\partial \overline{\rho H}}{\partial x} & \overline{\rho H} \geq \overline{\rho H}_{PMP} \end{cases} \tag{3.21}$$

Since we are considering a 1D horizontal scenario with $\theta_{PMP} = 0^oC$, $\frac{\partial \theta_{PMP}}{\partial x} = 0$. With Specific Enthalpy as the state variable, our initial conditions can be viewed on the left as temperate ice with 100% liquid water fraction and cold ice at -10^oC on the right. Specific Enthlapy is specified with the equation:

$$\overline{\rho H} = \left(1 - \phi_w\right) \rho_i C_i \theta + \phi_w \rho_w \left(C_i + L\right) \tag{3.22}$$

where we assume liquid water is at 0^oC. The large jump in $J_{conduction}$ causes the equation to be nonlinear, but it can be solved fully implicitly with a tridiagonal solve of $\overline{\rho H}$ and update of $J_{conduction}$ inside a Picard iteration loop. It is also of note that the finite difference form of $\frac{\partial}{\partial x}\left(J_{conduction}\right)$ is:

$$\frac{\partial}{\partial x}\left(J_{conduction}\right) = \alpha_{i+1/2} \frac{\left(\overline{\rho H}_{i+1} - \overline{\rho H}_i\right)}{\Delta x^2} - \alpha_{i-1/2} \frac{\left(\overline{\rho H}_i - \overline{\rho H}_{i-1}\right)}{\Delta x^2} \tag{3.23}$$

For the half-node diffusivity, a harmonic average is used between two nodes:

$$\alpha_{i+1/2} = \frac{2}{\frac{1}{\alpha_i} + \frac{1}{\alpha_{i+1}}} \tag{3.24}$$

At the ice-water interface, this results in the value of α being skewed toward α_0, the smaller of the two diffusivities. This value of α_0 controls the rate at which refreezing occurs, so can be varied until it matches the rate found with other methods described in this section.

3.5 Comparison of Refreezing Rates

The test case was run with all of the refreezing methods. For the numerical methods, the key parameter in each was varied over a range of values. See Table 3.1.

Method	Key Variable Value	Refreezing Time (years)
Analytical		6.822
CTS Tracking	$dt_1 = 1$ day	5.145
	$dt_1 = 10$ days	6.245
	$dt_1 = 50$ days	7.777
Apparent Heat Capacity	$\Delta\theta = 0.5^oC$	5.863
	$\Delta\theta = 0.1^oC$	6.192
	$\Delta\theta = 0.05^oC$	6.356
	$\Delta\theta = 0.01^oC$	6.493
Enthalpy Gradient	$K_0 = \frac{K_i}{25}$	5.233
	$K_0 = \frac{K_i}{50}$	5.918
	$K_0 = \frac{K_i}{100}$	6.712
	$K_0 = \frac{K_i}{500}$	11.506

Table 3.1: Comparison of refreezing times using four methods. For the numerical simulations, one parameter controls the refreezing rate and is varied.

We see that with the various methods of calculating refreezing time, the value spans from 5.145 years to 11.506 years. The analytical solution, which we will consider as the most accurate solution, falls in the middle at 6.822 years. Since the Enthalpy Gradient Method is being adopted in the 2D high resolution crevasse model, we are most interested in matching the value of α_0 that results in a refreezing rate close to the analytical solution. $\alpha_0 = \frac{\alpha_i}{100}$ results in a refreezing rate of 6.712 years, a 1.6% difference from the analytical solution. Since the analytical solutions is approximate and our value of γ resulted in a 3.6% error in Equation 3.17, this value of α_0 seems reasonable and will be adopted for the following sections.

Chapter 4

2D High Resolution Modeling Framework

4.1 Model Framework

As stated in Section 1.7, the goals of high-resolution modeling of the Cryo-Hydrologic System (CHS) include understanding the patterns and dominant processes associated with the advection and conduction of persistent englacial water. In this section, we describe our conceptual framework for modeling energy transfer from the CHS to the cold background ice. We conceptualize the CHS as composed of discrete elements such as crevasses, conduits, fractures and voids, embedded within the background ice. We consider typical horizontal extents over which meltwater generation rates are homogeneous, to be on the order of a few kilometers, and the spacing between meltwater entry points into the CHS (e.g. crevasse spacing) to be at least an order of magnitude smaller. Crevasses typically occur at fixed locations determined by the stress field within an ice sheet. Moulin and conduit-dominated CHS develop from crevasses that are advected out of crevasse fields [22, 37]. Thus, it is reasonable to view any fixed region within the wet snow zone or ablation zone, whose areal extent is of the order of a square kilometer, as an Eulerian "control volume" that contains a more or less temporally invariant array of CHS elements (as the most downstream element in the array is advected out of the control volume, another appears upstream). See Figure 4.1 for a schematic of the modeling framework. For simplicity, we assume an array of regularly spaced identical CHS elements. Of course, the nature of the array will vary from location to location, with crevasse fields in some locations, moulin-conduit complexes at other locations, or mixtures of both types, or even no CHS in some locations. Our objective is to quantify the warming influence

(i.e. CHW) of the CHS array on the "background" cold ice within the control volume. While CHW, increased ice velocities, and the increased meltwater generation at the surface may induce transformations in the CHS structure [12], we will not consider these feedback mechanisms. We also do not take into account the thermomechanical changes that take place in the background ice as a result of CHW. Phillips et al. [33] performs a thorough investigation of this.

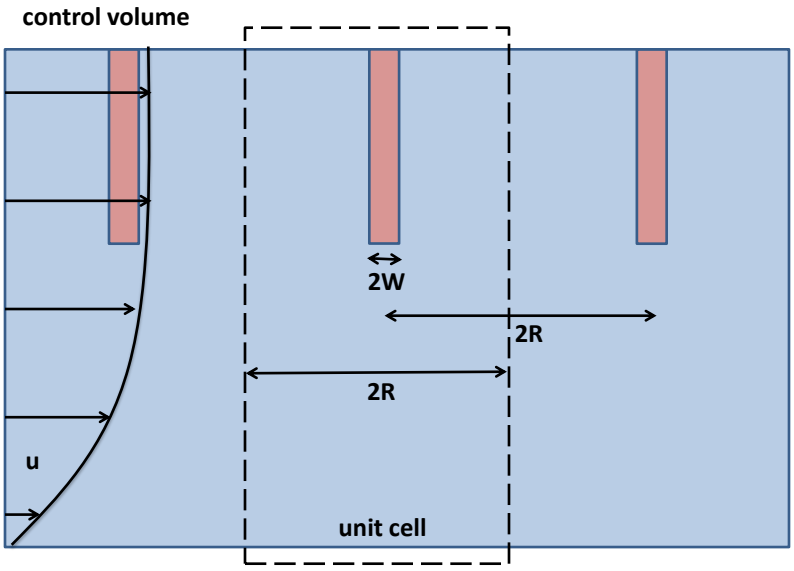

Figure 4.1: Schematic of modeling framework showing Eulerian unit cell, assigned velocity profile, and crevasse geometry. The domain is a 2D cross-section with the crevasse going into and out of the page.

The warming influence of englacial water is no doubt dependent on the physical and geometric properties of the CHS array, and establishing their inter-relationship is an important step in parameterizing CHW for use in large-scale ice sheet models. It is tempting to suggest that once their inter-relationship is established, CHW parameterizations can be developed by using high-resolution surface imagery to characterize the physical and geometric properties of the CHS array. However, some caution is warranted - while the internal geometry of the CHS at depth is related to its surface expression, it could be much more complex topologically, plausibly even exhibiting

multidimensional connectivity between CHS elements. In principle, our modeling approach can be extended to incorporate probabilistic variations in the structure of individual CHS elements and spacing between them. However, we believe that useful first-order insights are obtained even with our simplified representation. Furthermore, few if any detailed observations of the internal geometry of the CHS at depth are available to guide more sophisticated representations. Our approach to quantifying CHW is based on the following thought experiment: As an initial condition, consider that the Eulerian control volume in question was not experiencing any meltwater inputs. Assume that the onset of meltwater generation on the ice surface in the control volume rapidly leads to the development of a CHS array. We are now interested in heat transfer from the CHS to the background ice. For a regular array of CHS elements subject to synchronous meltwater inputs, we expect periodic temperature/enthalpy variations within the background ice. Thus it suffices to consider thermodynamic interactions between the CHS and background ice within one "unit cell" within the regular array of CHS elements [42]. During the active melt season, the thermodynamics of the CHW may be described by multi-dimensional generalizations of the Spring-Hutter equations [36] coupled with fracture propagation equations [40, 1]. However, the active melt season is typically short in duration [38], and for this reason we focus on energy transfer from retained meltwater in the CHS, which is the prevalent mechanism for most of the time since initiation of meltwater inputs. The retained meltwater is assumed to be stagnant, and our modeling approach focuses on computing the transfer of energy from liquid water retained in the CHS to the background ice as it freezes. The duration over which the liquid water in the CHS refreezes is determined by the dimensions of and spacing between the CHS elements, and the initial temperature of the background ice. As noted by Jarvis et al. [26], liquid water can persist for 20-30 years in large crevasses.

4.2 Choice of Modeling State Variable

We were presented with several choices of ways to model the advection-conduction equation for the 2D Crevasse system defined above. Namely, we explored the Enthalpy Gradient Method, the Apparent Heat Capacity Method, and a temperature-based Interface-Tracking Method. The use of

a unit cell of an Eulerian control volume as our modeling domain and a non-uniform velocity field quickly ruled out the Interface-Tracking Method because of the geometric complexity of tracking the interface in that system. Jarvis et al. [26] were able to use this approach because of their choice to use a Lagrangian control volume around the crevasse and a conduction-only refreezing scenario.

The Apparent Heat Capacity Method is a feasible apporach to handle the advection-conduction equation described here because it requires no tracking of an ice-water interface, it can be done semi-implcitly, has a tractable way of defining ice, water, and their thermal interaction, and has been shown to capture refreezing rates of liquid water in cold ice. The main drawbacks of this method, however, are that it has no physical basis for its linearization of conductivity and has no rigid way of conserving energy. Whereas the Enthalpy Gradient Method uses specific enthalpy as the state variable and accounts for all enthalpy in the system as refreezing occurs, the Apparent Heat Capacity Method uses temperature as the state variable and uses a false $\Delta\theta$ to account for liquid water and the conductivity. Whereas the Enthalpy Gradient method accounts for a Darcy-like movement of liquid water through ice, the Apparent Heat Capacity method treats diffusion of liquid water and ice as a mixture problem, using a linear interpolation of their diffusivities. In reality, a node may have both liquid water and ice, and the enthalpy of the node can be represented as an average of their enthalpies, but there is no homogeneous mixture of liquid water and ice that warrants the averaging of their conductivities. In terms of energy conservation, the false $\Delta\theta$ is problematic in that temperate ice and liquid water at the pressure melting point should have the same temperatue and experience no conduction, but the Apparent Heat Capacity approach defines temperate ice and liquid water at the pressure melting point to be separated by a temperature $\Delta\theta$.

The Enthalpy Gradient Method is also a feasible approach for many of the same reasons. It requires no tracking of an interface, it can be done semi-implicitly, and it has been shown to capture the refreezing rate of liquid water in cold ice reasonably. Its main advantage over the Apparent Heat Capacity Method is that it is an energy conserving method and has a physical justification (however poorly constrained) for diffusion of liquid water through ice. This is very important due to our modeling goals for this problem. Namely, we are interested in starting with an initial

distribution of liquid water in a cold ice sheet and determining the long-term spatial distribution of heat resulting from the melt-water input. As we are using an Eulerian control volume approach, it is very important to track any inputs and outputs to the system so that energy is not erroneously lost or gained over the course of the simulation.

The main drawback of using the Enthalpy Gradient Method is that in using Specific Enthalpy as the state variable, there is initially a very large jump in the initial conditions between the Specific Enthalpy of liquid water and the cold ice background. For background ice at -10^oC, the initial jump in Specific Enthalpy is $\overline{\rho H}_{liquid\ water} - \overline{\rho H}_{cold\ ice} = \rho_w \left(C_i \theta_{PMP} + L\right) - \rho_i C_i \left(-10^oC\right)$. This is important becuase at early times, conduction across this large gradient, while controlled by α_0, the temperate diffusivity, causes outward growth of the temperate ice around the crevasse. While not nonphysical, we tend to see a greater outward growth of temperate ice using the Enthalpy Gradient Method than other methods (as seen in the Refreezing Rate section) before refreezing occurs. We can choose α_0 that matches other methods' total refreezing times, however, as this is what we are most concerned with. In the 1D Refreezing Rate section (section 3.5), we found that the timescale of temperate ice outward growth is on the order of months while the timescale of crevasse refreezing is on the order of years or decades.

4.3 Computational Approach

Energy transport is modeled using the Advection-Conduction equation appropriately linearized using an enthalpy, or polythermal, method [2]. While conduction in cold ice simply follows Fourier's Law, the residual heat flux in temperate ice is the sum of a conductive and latent heat flux. The conductive heat flux arises from differences in the surface elevation of adjacent ice nodes, and hence the pressure melting point temperature, which we will neglect in our modeling framework. The latent heat flux arises from non-advective liquid water diffusion. Aschwanden et al. [2] reasoned that a Fick-type diffusion of liquid water made sense for a small liquid water content, but our model will encounter liquid water fractions as large as 1 during the melt season, and large liquid water contents even during the winter. While other parameterizations for liquid water flux

have been suggested [25, 16], no good laboratory or field data exists to corroborate any particular choice. We therefore choose to adopt:

$$q_l = -\alpha_0 \nabla \overline{\rho H} \tag{4.1}$$

where q_l is the latent heat flux and α_0 is a constant small diffusivity. With large liquid water fractions, and hence large gradients in specific enthalpy, q_l is sensitive to the choice of α_0. We therefore performed a sensitivity analysis on the value of α_0 in the enthalpy method in order to find a value that results in the same refreezing rate of a liquid water body in cold ice obtained from an analytical solution and CTS-tracking numerical solution (see section 3.5). We found that the refreezing rate using the enthalpy method with $\alpha_0 = \frac{\alpha_i}{100}$ where α_i is the diffusivity of cold ice matches the analytical and CTS-tracking numerical solutions well. This results in the following expression of the Advection-Conduction Equation:

$$\frac{\partial \overline{\rho H}}{\partial t} + \vec{u} \cdot \nabla \overline{\rho H} - \nabla \cdot (J_{conduction}) = Q \tag{4.2}$$

$$J_{conduction} = \begin{cases} \alpha_i \nabla \overline{\rho H} & \overline{\rho H} < \overline{\rho H}_{PMP} \\ \alpha_0 \nabla \overline{\rho H} & \overline{\rho H} \geq \overline{\rho H}_{PMP} \end{cases} \tag{4.3}$$

where $\vec{u}$ is the velocity vector and J is the conductive heat flux.

To solve the Advection-Conduction equation with the Enthalpy Gradient Method, the domain is discretized using the finite volume method in 2D. See Figure 4.2 for a schematic of the positive flux directions in a node. The state variable, Specific Enthalpy, is solved at the center of each node. Conduction and advection are accounted for by tracking fluxes across node boundaries, as shown with arrows in Figure 4.2. As such, diffusivity is calculated at the node boundaries as the harmonic average of the diffusivities of the adjacent nodes. For cold ice, $\alpha = \alpha_i$ and for temperate ice, $\alpha = \alpha_0$. The harmonic average is used because at a cold-temperate interface, the averaged boundary value of diffusivity will be skewed toward the smaller diffusivity, α_0. As for velocity values at the node boundaries, the mean of the two adjacent nodes is used.

To solve the Advection-Conduction Equation using the Enthalpy Gradient Method in 2D, operator splitting was used to solve for the horizontal conduction, vertical conduction, and vertical

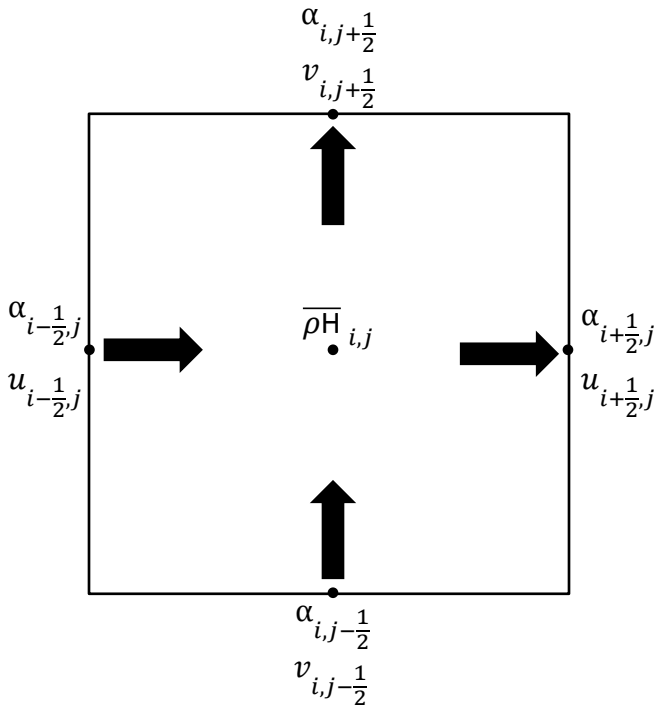

Figure 4.2: Finite volume cell at location (i,j). The cell is width Δx and height $\Delta \zeta$. The arrows show the direction of positive flux across cell boundaries. Velocity and diffusivity are calculated at the half-node spacing with a harmonic averaging.

advection in one half-timestep and the horizontal advection in the next half-timestep. In the conduction and vertical advection half-timestep, the solution for a node was dependent on the four adjecent nodes and itself. As shown in Equation 4.4, the conduction is solved semi-implicitly by keeping the diffusivity lagged 1 timestep (explicit) while solving for Specific Enthalpy implicitly. The vertical advection is solved with an explicit upwinding scheme. This results in the first half-timestep having a 5-node implicit dependency, which can be solved using a sparse 5-banded matrix

solver. Matlab's sparse backslash was used to solve this.

$$\left[\frac{\overline{\rho H}_{i,j}^{n+\frac{1}{2}} - \overline{\rho H}_{i,j}^{n}}{\Delta t}\right]\Delta x_i \Delta y_j - \alpha_{i-\frac{1}{2},j}^{n}\left(\frac{\overline{\rho H}_{i-1,j}^{n+\frac{1}{2}} - \overline{\rho H}_{i,j}^{n+\frac{1}{2}}}{\frac{\Delta x_i + \Delta x_{i-1}}{2}}\right)\Delta y_j - \alpha_{i+\frac{1}{2},j}^{n}\left(\frac{\overline{\rho H}_{i+1,j}^{n+\frac{1}{2}} - \overline{\rho H}_{i,j}^{n+\frac{1}{2}}}{\frac{\Delta x_i + \Delta x_{i+1}}{2}}\right)\Delta y_j$$
$$-\alpha_{i,j-\frac{1}{2}}^{n}\left(\frac{\overline{\rho H}_{i,j-1}^{n+\frac{1}{2}} - \overline{\rho H}_{i,j}^{n+\frac{1}{2}}}{\frac{\Delta y_j + \Delta y_{j-1}}{2}}\right)\Delta x_i - \alpha_{i,j+\frac{1}{2}}^{n}\left(\frac{\overline{\rho H}_{i,j+1}^{n+\frac{1}{2}} - \overline{\rho H}_{i,j}^{n+\frac{1}{2}}}{\frac{\Delta y_j + \Delta y_{j+1}}{2}}\right)\Delta x_i$$
$$+\overline{\rho H}_{i,j}^{n} u_{i+\frac{1}{2},j}\Delta y_j - \overline{\rho H}_{i-1,j}^{n} u_{i-\frac{1}{2},j}\Delta y_j = Q_{i,j} \tag{4.4}$$

Horizontal advection was solved using a Method of Characteristics scheme modified for front tracking. This is done because when modeling the CHS, there is a large jump ($\approx$ 2 orders of magnitude) in enthalpy from a crevasse to the background cold ice. Most advection schemes struggle to maintain a sharp front and suffer from numerical dispersion, so a scheme was chosen that would maintin the sharp front. This is done by using the Method of Characteristics with a nearest-neighbor interpolation and a front-tracking algorithm that takes advantage of the fact that horizontal velocity remains spatially and temporally constant within a model row. In other words, the Specific Enthalpy of a node is advanced forward a full node only when sufficient time-steps it have elapsed such that $\frac{u\ it\ \Delta t}{\Delta x} = 1$ where u is the horizontal velocity and Δt is the timestep.

Finally, a non-dimensional vertical ζ is used:

$$\zeta = \frac{z - z_b(x)}{z_s(x,t) - z_b(x)} \tag{4.5}$$

where z_b is the bedrock elevation and z_s is the surface elevation. This ensures that each model column has the same number of nodes and that a constant vertical spacing $\Delta\zeta$ can be used.

4.4 Velocity Profiles

In our 2D model, we elected not to have a thermomechanical coupling between temperature and velocity. Instead, we derive a horizontal velocity profile using the non-linear constituative relation given by Glen's flow law combined with the Shallow Ice Approximation which reduces the stress tensor to only leading order terms resulting from assuming simple shear. See Section 1.4 for

a derivation of these values. An initial value for A was calculated based on Equation 1.2. This equation for horizontal velocity can be transformed to the ζ coordinate system:

$$u(x,\zeta) = H^{n+1}\frac{2A}{n+1}\left(\rho g sin\alpha_{slope} - \frac{\partial z_s}{\partial x}\right)^n \left(1-(1-\zeta)^{n+1}\right) \tag{4.6}$$

where H is the ice height. A simple linear approximation for vertical velocity is used where the surface velocity is assumed to be equal to the ablation rate at the surface and 0 at the bed. Equation 4.7 shows this velocity scaled for the non-dimensional ζ coordinate system.

$$w'(x,\zeta) = -\frac{1}{H}\frac{b}{\zeta} \tag{4.7}$$

where b = ablation rate.

4.5 Strain Heating

An equation for strain heating was derived in Section 1.4 using the Shallow Ice Approximation and Glen's Flow Law. Like velocity, strain heat can be transformed to the ζ coordinate system:

$$Q(\zeta) = 2A\left(\rho g H \alpha_{slope}\right)^{n+1}(1-\zeta)^{n+1} \tag{4.8}$$

4.6 Initial Temperature Distribution

A steady-state column model was used to develop an initial background ice temperature profile. The steady-state Advection-Conduction equation was written out for each column in the domain and employed a horizontal advection parameterization to account for advective cooling coming from upstream of the domain:

$$w'(\zeta)\frac{\partial\overline{\rho H}}{\partial\zeta} - \frac{1}{H^2}\frac{\partial}{\partial\zeta}\begin{pmatrix}\alpha_i\frac{\partial\overline{\rho H}}{\partial\zeta}\\ \kappa_i\frac{\partial\theta_{PMP}}{\partial\zeta}+\alpha_0\frac{\partial\overline{\rho H}}{\partial\zeta}\end{pmatrix} = Q(\zeta) - u(\zeta)\rho C\alpha_{slope}\lambda \tag{4.9}$$

A Picard iteration was performed until convergence was met. We adjusted the values of Q and u until the profile matched 1990 temperatures for Sermeq Avannarleq near the ELA [39]. Since our modeling framework assumes that the unit cell of our domain is horizontally homogeneous, we can assume that each column in our domain initially has the same temperature profile. Columns that

initially are crevassed have the specific enthalpy in those crevassed nodes replaced with the crevasse specific enthalpy.

4.7 Boundary and Initial Conditions

An Eulerian framework was used to model a Cryo-Hydrologic System with crevasse spacing R and periodic boundary conditions at the upstream and downstream columns. Initially, the background ice has temperature of the steady-state column model and the crevasse is filled with liquid water at $\theta = \theta_{PMP}$. This one-time filling of liquid water is then allowed to refreeze. In terms of the state variable, specific enthalpy, the background ice initial condition is:

$$\left(\overline{\rho H}_{ice}\right)_0 = \rho_i C_i \theta_{ss} \tag{4.10}$$

where θ_{ss} is the steady-state temperature and comes from Equation 4.9 where specific enthalpy is converted back to temperature with Equation 2.11. See Figure 4.3 for a plot of the initial temperatures.

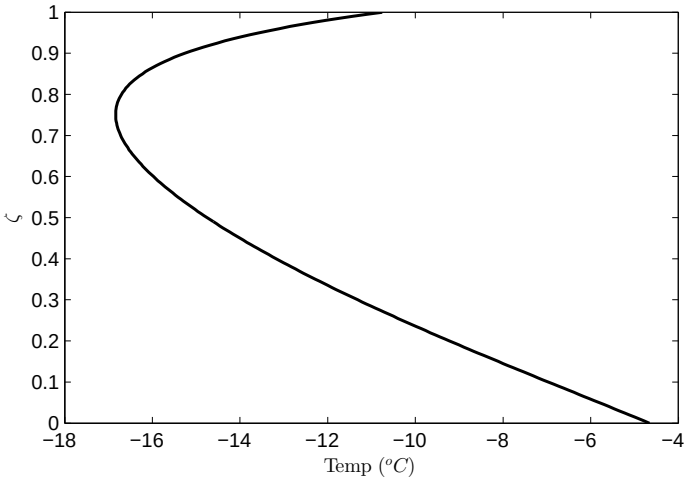

Figure 4.3: Initial Steady-State Column Model Temperatures for the TD5 pre-CHW scenario

The initial specific enthalpy of the crevasse nodes is:

$$\left(\overline{\rho H}_{crevasse}\right)_0 = \overline{\rho H}_{PMP} + \left(\rho_w - \rho_i\right) C_i \left(\theta_{PMP}\right) + \rho_w L \tag{4.11}$$

where $\overline{\rho H}_{PMP}$ is the specific enthalpy of ice at $\theta = \theta_{PMP}$ with no liquid water fraction, ρ_w is the density of water, ρ_i is the density of ice, and L is the latent heat of fusion. The boundary condition for the top row of the domain is:

$$\overline{\rho H}_{top} = \rho_i C_i \theta_{air} \tag{4.12}$$

where θ_{air} is a sinusoidal function that oscillates between the average maximum summer temperature and average winter minimum temperature at the TD5 weather station on Sermeq Avannarleq. Summer temperatures above 0^oC were set to 0^oC as it was assumed that all generated surface melt runs into a crevasse. The bottom boundary condition is:

$$\frac{\partial \overline{\rho H}}{\partial \zeta}_{bottom} = \begin{cases} \frac{-1}{H^2}\frac{G}{\alpha_i} & \text{cold basal layer} \\ 0 & \text{positive-thickness temperate basal layer} \end{cases} \tag{4.13a}$$

$$\overline{\rho H}_{bottom} = \overline{\rho H}_{PMP} \text{ zero-thickness temperate basal layer} \tag{4.13b}$$

where $G = 0.0502\frac{J}{s\ m^2} = 1.2\ HFU$ is the average geothermal heat flux found in Western Greenland. In the cold basal temperate layer case, the geothermal heat flux causes a rise in temperature at the bed. In the zero-thickness temperate basal layer case, a Type-1 boundary condition must be used to hold $\overline{\rho H}_{bottom} = \overline{\rho H}_{PMP}$ while a basal temperate layer is established. Failure to use this boundary condition results in an oscillation of the bottom node between a temperate and cold condition. Finally, the positive-thickness temperate basal layer case arises from the assumption that in temperate conditions, the geothermal heat flux is entirely consumed by basal melt. While our model does not track mass loss, this boundary condition is still appropriate for solving the energy equation.

The periodic boundary conditions are applied to the left and right columns of the unit cell and can be expressed with Equation 4.14.

$$\overline{\rho H}_{left} = \overline{\rho H}_{right} \tag{4.14}$$

4.8 Fracturing and Draining

Hydrofracturing of ice that drives water through cracks and fractues involves a complex interaction of the ice sheet stress field, hydrostatic pressure, melt water generation, and ice sheet thermodynamics. To evaluate the thermal influence of a fracturing event similar to Boon et al. [4], i.e. stagnant water trapped in stress-induced fractures, four different methods that employed the random-walk method were used to distribute a filled crevasse's worth of liquid water into a fracture network annually and allowing it to refreeze. The thermal influence of each type of fracturing includes the magnitude of warming and characteristic areal scale of influence under a creasse following a draining event.

To implement the four different methods, a fracture width is assigned and a random walk method is used to route the fracutre network until all of the water that is retained has been routed. In subsequent melt seasons, the shallow creavsse is allowed to fill and drain its liquid water again into the existing or newly created network. See Figure 4.6 for a general schematic of the filling and draining scenario. See Section 4.9 for a description of the four different methods for creating the fracture network.

4.9 Modeling Scenarios

There are three main modeling scenarios we consider as end-members for CHW. The first scenario is that of a shallow water-filled crevasse field with crevasses of width 2W separated by width 2R. A unit cell in the field captures a crevasse surrounded by background ice of width 2R. The crevasse penetrates 1/3 the thickness of the ice and the ice thickness is chosen to be $H = 500m$. See Figure 4.4 for a schematic of the shallow crevasse scenario. In order to explore different initial conditions and the effect on CHW, we vary crevasse width, crevasse spacing, and the initial background ice temperature and allow the model to run until the crevasse refreezes and steady-state temperature is reached.

The next scenario considered is a field of deep, but not fully penetrating water bodies. The

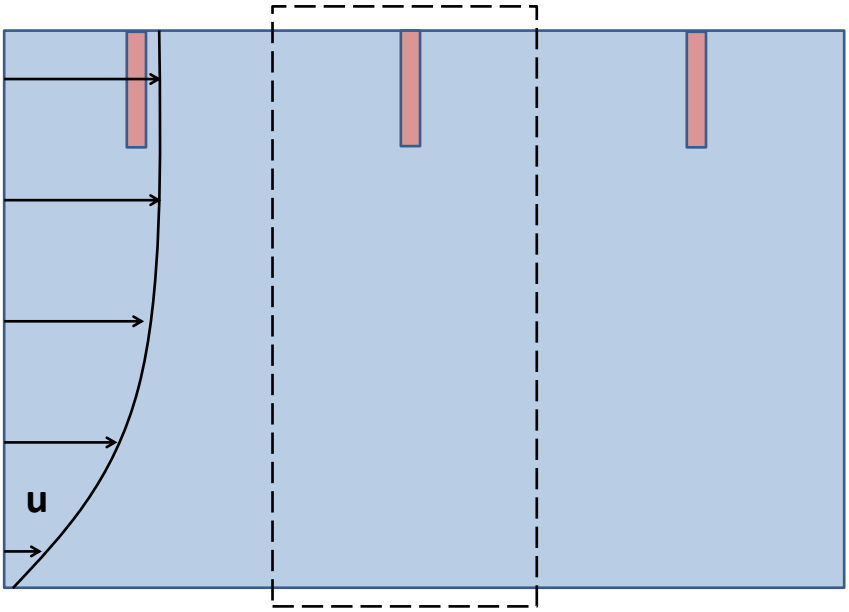

Figure 4.4: Shallow crevasse modeling scenario with a one-time filling of an upstream crevasse that is part of a series of crevasses. The crevasse width is 2W and the spacing between crevasses is 2R.

same geometric parameters are varied as the shallow crevasse case. Whereas a constant background ice temperature is used in the shallow crevasse field case, a more realistic steady-state temperature profile that does not include the effects of CHW is assigned for the initial background ice temperature field. This temperature field is modeled to match pre-CHW conditions at the TD5 borehole site on the Sermeq Avannarleq glacier in Western Greenland [39]. The ice sheet thickness is also increased to $H = 950m$. While shallow crevasses experience a nearly constant horizontal velocity from top to bottom, deep water bodies penetrate to the depth of the ice sheet where a significant horizontal velocity gradient exists. We therefore compare warming from a case with no horizontal velocity to a full conduction-advection case to isolate the effects of the horizontal velocity gradient at depth. These effects include stretching of the initially rectangular water body and the added effects of strain heat and advective cooling from upstream ice. See Figure 4.5 for a schematic of the deep water-filled water body case.

The final scenario involves the most complex and dynamic geometry. A shallow water-filled

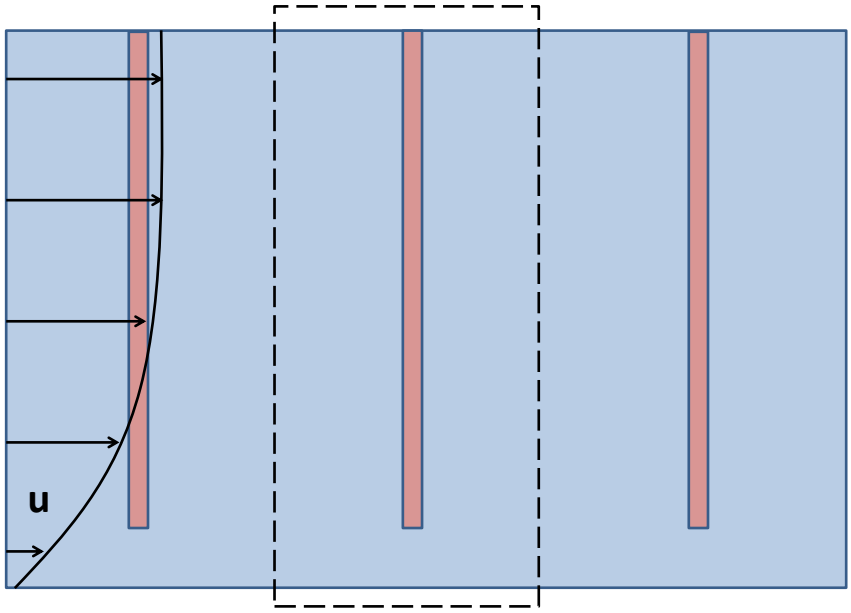

Figure 4.5: Deep water body modeling scenario with a one-time filling of an upstream crevasse that is part of a series of crevasses. The crevasse width is 2W and the spacing between crevasses is 2R.

crevasse fills during the melt season and is then allowed to drain into a fracture network over the winter. This crevasse filling and fracturing occurs annually. Since mechanical fracture formation and subsequent hydrofracturing in cold ice are poorly understood phenomena, we choose to constrain the fracture network in five different ways that highlight and contrast different mechanisms for crevasse fracturing.

In the first three of the filling and fracturing scenarios, a random walk method is used to route 25% of the crevasse's liquid water into the CHS. A characteristic fracture length and width are assigned, and fractures branch from the crevasse or existing fractures laterally or downward until 25% of the creavsses's water is routed. Realistically, only a portion of the liquid water that fills a crevasse will be retained in the CHS long enough to refreeze and release latent heat. The three scenarios differ in the depth to which the random walk algorithm allows the CHS to extend. In the first scenario, the CHS depth is unbounded and water-filled fractures are allowed to form at any depth. In the second scenario, fractures are permitted to route water only in the top half of

the ice sheet. The third scenario limits fracture creation the greatest to only the top third of the ice sheet. It should be noted that the same enthalpy is routed annually in these three scenarios, so limiting the fracture extent will cause greater warming in a more concentrated area.

In the fourth and fifth scenarios, the heterogeneity of a randomly generated fracture network is eliminated and instead a characteristic rectangular area under the crevasse is uniformly warmed. In the results shown here, the rectangular area is positioned under the crevasse and extends to $\frac{5}{6}$ of the ice sheet depth. These two scenarios differ in the width of characteristic rectangular area: in the fourth scenario, the width is 20m and in the fifth scenario, the width is 50m. These two scenarios also differ from the first three in the amount of enthalpy routed to the CHS annually. Instead of using the crevasse area to determine the volume of liquid water routed to the CHS, an ablation rate is used. We assume an ablation rate of $2\frac{m}{a}$, 75% of which runs off the surface or drains to the bed. The remaining liquid water is routed to the CHS and is equivalent to adding the enthalpy of roughly 0.05% of the ice sheet's volume as liquid water annually.

In all of the fracturing scenarios, a crevasse width of $2W = 2m$, crevasse spacing of $2R = 100m$, and ice sheet depth of $H = 950m$ are used. The crevasses penetrate 1/3 the thickness of the ice sheet. See Figure 4.6 for a general schematic of the filling and draining scenarios 1-3, Figure 4.7 for a general schematic of the filling and draining scenarios 4-5, and Table 4.1 for a description of all 5 fracturing scenarios.

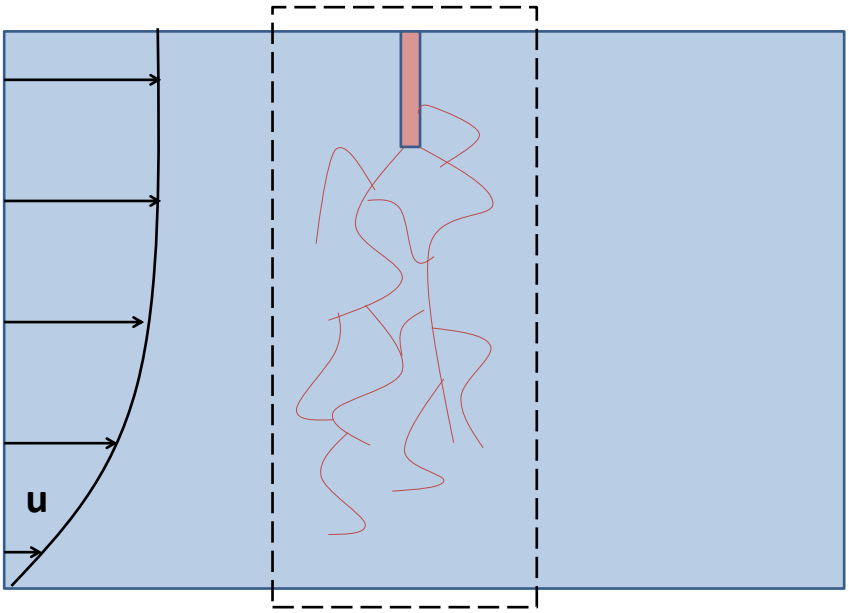

Figure 4.6: Fracturing modeling scenarios 1-3 with an annual filling and draining of a crevasse that is part of a series of crevasses. The crevasse width is 2W and the spacing between crevasses is 2R.

Filling and Draining Scenario	Description
1	random walk method to evolve fracture network annually unbounded depth of fracture network 25% of crevasse volume routed annually
2	random walk method to evolve fracture network annually fracture network limited to top $\frac{1}{2}$ of ice sheet 25% of crevasse volume routed annually
3	random walk method to evolve fracture network annually fracture network limited to top $\frac{1}{3}$ of ice sheet 25% of crevasse volume routed annually
4	homogeneous rectangular fracture zone fracture zone $20m$ wide 25% of $2\frac{m}{a}$ ablation rate routed annually
5	homogeneous rectangular fracture zone fracture zone $20m$ wide 25% of $2\frac{m}{a}$ ablation rate routed annually

Table 4.1: Descriptions of the 5 filling and draining scenarios used in our modeling framework

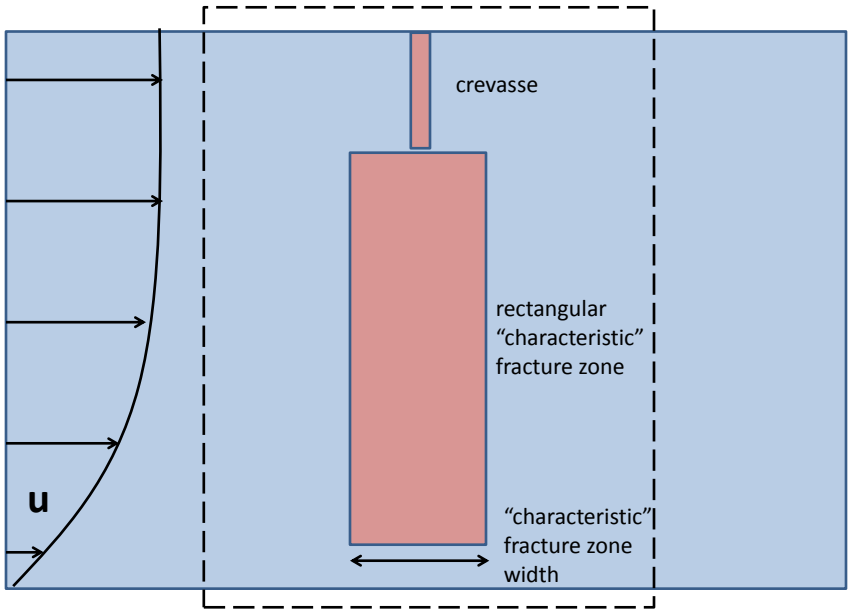

Figure 4.7: Fracturing modeling scenarios 4-5 with an annual filling and draining of a crevasse that is part of a series of crevasses. The crevasse width is 2W and the spacing between crevasses is 2R.

Chapter 5

2D CHW Modeling Results

There are three modeling scenarios investigated with the 2D CHS model framework: a shallow crevasse field, a deep penetrating crevasse, and dynamic draining and refilling of a crevasse into a fracture network. See Section 4.9 for details of each.

5.1 Potential Warming from conduction only

Average enthalpy in a 1D system can be found to determine ultimate potential warming from a crevasse. This assumes that heat transfer is only accomplished through horizontal conduction and advection and that the crevasse has frozen and a steady-state has been reached.

$$\theta_{final} = \frac{W\left(\overline{\rho H}\right)_{crevasse} + (R-W)\left(\overline{\rho H}\right)_{ice}}{\rho_i C_i R} \tag{5.1}$$

where W is the crevasse half-width and R is the crevasse half-spacing. This final temperature is only valid at the depths to which the crevasse penetrates.

5.2 Shallow Crevasse Modeling Results

As an example of CHW resulting from a shallow crevasse, we can use our modeling framework to examine a 1m wide crevasse that penetrates $\frac{1}{3}$ the depth of an ice sheet that is 500m deep and initially -10^oC. The crevasse is initially filled with water and is then allowed to refreeze. Figure 5.1 shows a progression of temperature as the crevasse refreezes and releases its latent heat. We also notice that because of the scaling, horizontal conduction is the dominant process that controls

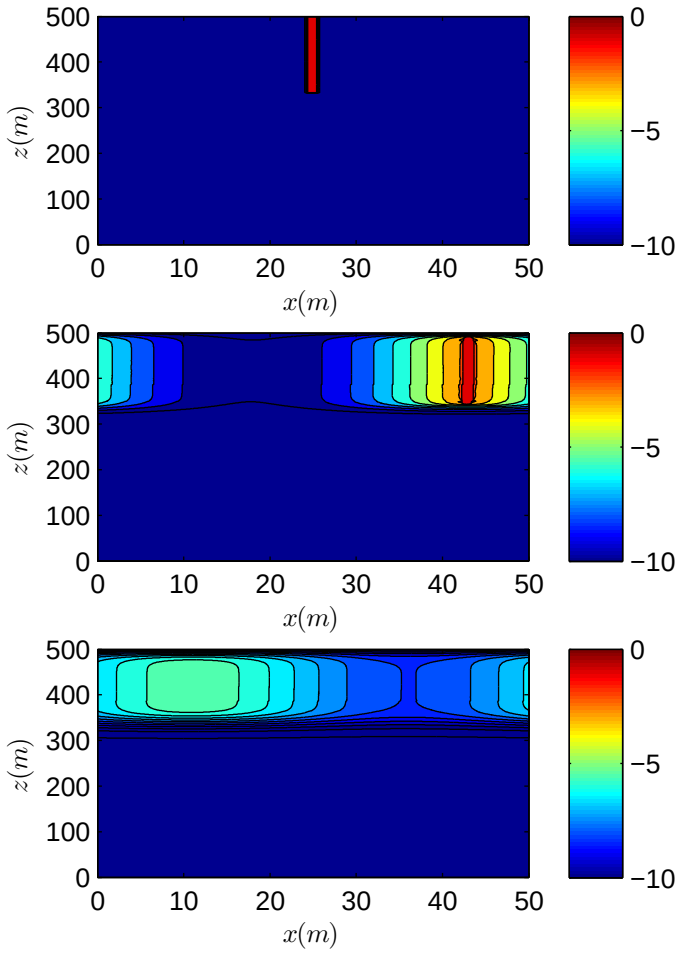

Figure 5.1: 2D plots of Shallow Crevasse refreezing. The top figure is the initial condition of a 1m wide crevasse and background ice at -10^oC. The middle figure is at t=2 years and shows warming of the background ice. The bottom figure is at t=4 years and shows that the crevasse has refrozen. The color bar is in ^oC.

the refreezing rate and dictates where heat moves in the system. The surface area of the side of the crevasse is much greater than the tip of the crevasse, and the spacing between crevasses is generally smaller than the length from the tip of the crevasse to the bed. To a shallow depth, Glen's Flow Law dictates that the horizontal velocity gradient is small and the crevasse maintains its original orientation. This results in most of the heat conducting in a 1D manner in the horizontal direction. As seen in Figure 5.2, the refreezing behavior of a shallow crevasse is controlled by

the crevasse width, crevasse spacing, and background ice temperature. Colder background ice and smaller crevasse width result in a faster refreezing time, while reducing the crevasse spacing results in longer persistence of liquid water in the crevasse. By nondimensionalizing the problem

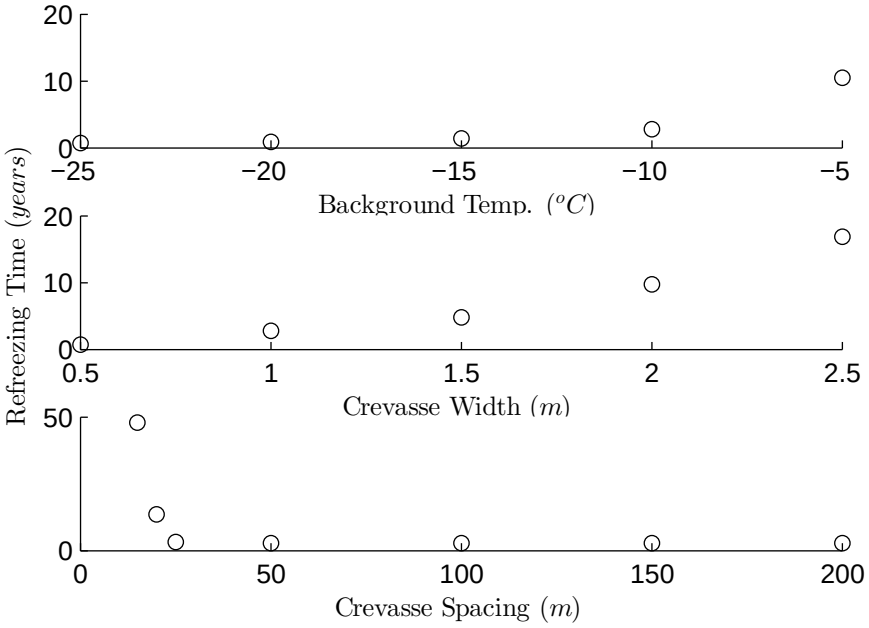

Figure 5.2: Refreezing time for a shallow crevasse compared to a base case of -10^oC background ice, 1m wide crevasse width, and 50m crevasse spacing.

using the crevasse width, crevasse spacing, and background ice temperature, we can derive 1D analytical solutions that approximate the horizontal conductive heating in front of the crevasse. See Chapter 6 for the derivation of these 1D analytical solutions and for the nondimensionalization. We can compare the warming in front of the crevasse at shallow depth to the warming predicted by the Fourier Series analytical solution by assuming that the moving phase change interface at the crevasse wall, which the numerical solution captures, can be approximated by a stationary phase change interface. Also, the Fourier Series solution is only valid at times less than the refreezing time of the crevasse. As we see in Figure 5.3, there is good agreement between the numerical and Fourier Series solutions in front of the crevasse. The agreement between the numerical results and analytical solutions confirm that the warming resulting from a shallow crevasse can be well

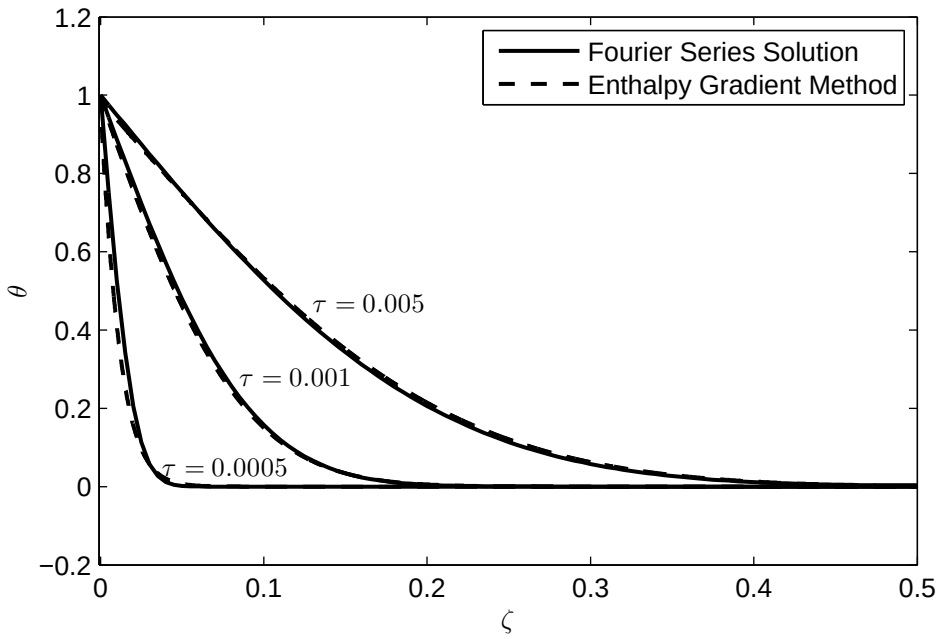

Figure 5.3: Non-dimensional warming profiles in front of a crevasse at nondimensional times $\tau = 0.0005$, $\tau = 0.001$, and $\tau = 0.005$. All times are before τ_f, the crevasse refreezing time, and show good agreement between the Enthalpy Method numerical solution and 1D Fourier Series Solution.

approximated by the assumption that heat is only conducted horizontally. This information will be used in Chapter 6 for construction of alternative CHW parameterizations. This further suggests that any significant thermomechanical influence from CHW at depth in the ice sheet can only be accomplished by a delivery of liquid water at depth - not through vertical advection or vertical conduction.

5.3 Deep Water Body Modeling Results

Many of the same insights from the shallow crevasse case can also be applied in the case of a deep-penetrating water body. Where the two differ is that a deep water body penetrates to the region of the ice sheet where significant horizontal velocity gradient exists in the vertical. This high strain rate at depth had several consequences on heat transfer in the lower ice sheet near the CHS. First, strain heat was generated from the velocity gradient and is a source of heat primarily at depth in the ice sheet. This strain heat was counteracted by the advective cooling parameterization,

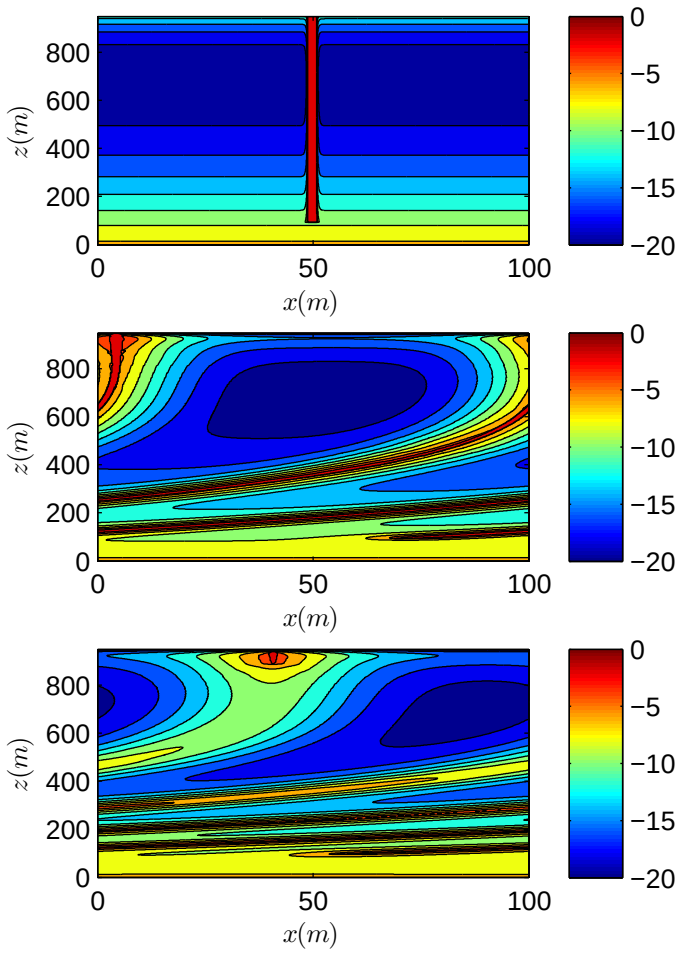

Figure 5.4: 2D plots of Deep Water Body refreezing. The top figure is the initial condition of a 1m wide crevasse. The middle figure is at t=3 years and shows warming of the background ice and stretching of the water body. The bottom figure is at t=5 years and shows that the upper portion of the water body has refrozen while the bottom persists as liquid water. The color bar is in ^oC.

however, and should not affect overall warming or time to refreezing for the CHS.

Stretching of the lower ice sheet also brought upstream and downstream water bodies closer together. In a conduction-only case (with no horizontal advection), a large water body spacing caused water bodies in a field to act thermodynamically independent. With stretching, however, initially thermodynamically disconnected elements were brought to a close distance where warming of the background ice caused conduction to slow for all the elements. See Figure 5.4 at $t = 3$ *years*

for an illustration of stretching. This phenomenon alone should cause increased persistence of liquid water as refreezing is slowed by upstream and downstream CHW.

While stretching of the deep water element brought upstream and downstream elements closer, it also increased the surface area of liquid water exposed to the surrounding cold ice. This phenomenon alone should cause refreezing to occur faster as there is greater contact area with cold ice and decreased cross-sectional area of the liquid water body.

As seen in Figure 5.5 the combined effects from stretching of the deep liquid water body caused it to refreeze faster than a case with horizontal velocity turned off. In our model setup with advection turned on, liquid water near the bed refroze almost 3 years faster than the case with horizontal velocity, strain heat, and advective cooling turned off. This means that the increase in liquid water surface area had a more important role in refreezing time than the liquid water elements being brought closer together and providing warming to upstream and downstream liquid water elements.

The water body stretching and reduced persistence of liquid water at depth may have several consequences on the ice sheet thermodynamics. Stretching increases the spatial extent of where a deep liquid water body can cause warming. The extended areal influence may be thermomechanically important as isolated pockets of warm ice won't cause as much ice acceleration as an extended area of warm ice. Conversely, stretching decreases the cross-sectional area of the liquid water body and decreases the amount of enthalpy available to refreeze and provide latent heat. This will cause the magnitude of warming to be lower than a case without stretching. A decrease in the refreezing time also decreases the likelihood of the liquid water draining to the bed. While we have not done a careful coupling of stress fields around liquid water bodies, other sources such as Van der Veen et al. and Clason et al. [40, 11] suggest that given sufficient time, liquid water will fully penetrate to the bed and drain. A faster refreezing rate will reduce the likelihood of this happening and provide a higher probability of CHW.

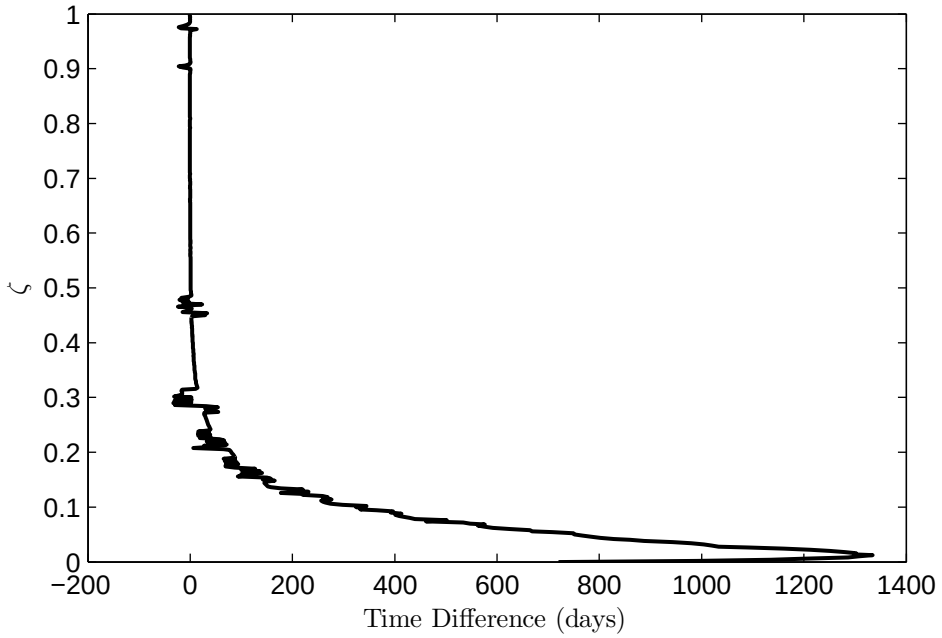

Figure 5.5: Difference in refreezing time of a deep 1m wide water body between a model run with horizontal advection and strain heat and a conduction-only scenario. Vertical advection and strain heat cause almost a 3 year decrease in refreezing time near the bed of the ice sheet.

5.4 Draining and Filling Modeling Results

Figure 5.6 shows a 2D plot of warming as a result of 40 annual filling and draining events of the crevasse in the unit cell using the 1st filling and draining scenario (see Section 4.9 and Table 4.1 for a description of the scenarios). While there was evidence of fractures from the most recent melt season providing up to 16^oC warming locally around the fractures, most of the background ice saw warming as the cumulative result of refreezing of water-filled fractures and conduction over 40 years. From roughly $\zeta = 0.5$ to $\zeta = 0.9$ there was warming of 7^oC to 10^oC far from the crevasse and warming of 12^oC to 16^oC in the 30m surrounding the crevasse. Even though scenario 1 had no bound on the depth of fractures, the bottom of the ice sheet from $\zeta = 0$ to $\zeta = 0.5$ experienced very little cumulative warming over 40 years - from 0^oC to 5^oC. While this scenario was the only one that allowed for fractures to penetrate all the way to the bottom of the ice sheet, we still saw that fracturing near the bed was a rare event and produced little thermomechanically significant

warming. The routing algorithm was certainly not rigorous, however, and could be tweaked to produce more warming at depth. Results shown here should not be regarded as predictive, but more as a bound on possibilities.

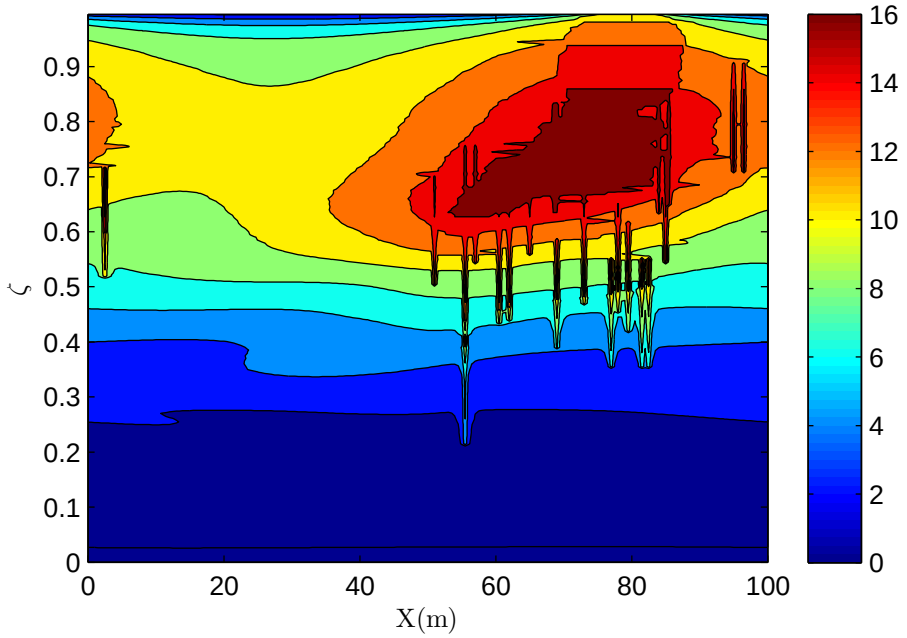

Figure 5.6: Final warming after 40 years of draining and fracturing of crevasse using scenario 1. 25% of crevasse water is retained. The contours are ^oC warming.

Figure 5.8 shows vertical temperature profiles $20m$ in front of the crevasse for the 5 filling and draining scenarios. Scenario 1 showed progressive warming of the top $\frac{1}{3}$ of the ice sheet at each timestep plotted. After 30 years, the top $\frac{2}{3}$ of the ice sheet experienced significant warming as more fractures were routed to $\zeta = 0.3$ to $\zeta = 0.6$ between years 10 and 30. This was a result of the fracture routing algorithm: as nodes in the vicinity of the crevasse became temperate, those nodes would no longer be available for fracturing in the future.

Scenarios 2 and 3, shown in figures 5.8b and 5.8c respectively showed similar patterns of warming, but showed little to no warming below the threshold depth where fractures could be routed. In scenario 3, we see that there is only warming above $\zeta = 0.6$, but that the warming was greater than scenarios 1 and 2. Even $20m$ in front of the crevasse, there were temperate nodes after

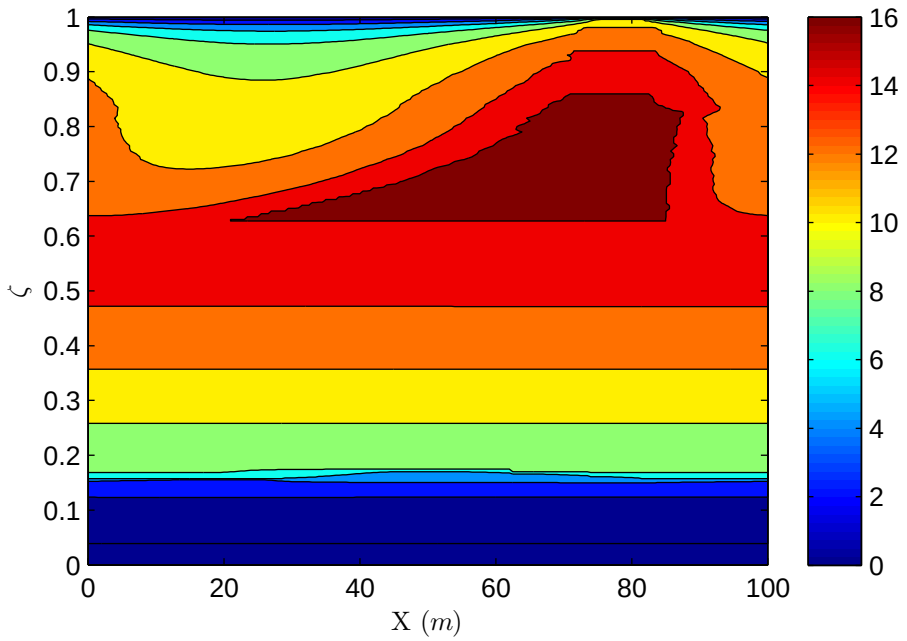

Figure 5.7: Final warming after 40 years of draining and fracturing of crevasse using scenario 4. 25% of $2\frac{m}{a}$ ablation rate is retained. The contours are ^oC warming.

30 years of filling and draining in scenario 3. Scenarios 2 and 3 also show that vertical conduction is a poor mechanism for transporting heat to depth. Even with a sharp temperature gradient at the drainage threshold depth, there was little warming below $\zeta = 0.5$ and $\zeta = 0.66$ for scenarios 2 and 3 respectively.

Scenarios 4 and 5, shown in figures 5.8d and 5.8e respectively showed more uniform warming from $\zeta = 0.1$ to $\zeta = 0.8$ than scenarios 1-3 because of the mechanism used to route enthalpy annually. Scenario 4 used a $20m$ wide fracture zone below the crevasse, so the vertical profiles shown $20m$ in front of the crevasse corresponded to a vertical profile $10m$ outside of the fracture zone. This meant that all warming shown was a result of conduction across $10m$ of background ice. As such, there was very little warming after 5 years from $\zeta = 0.2$ to $\zeta = 0.8$, the depth of the fracture zone. There was, however, 2^oC warming after 5 years from $\zeta = 0.8$ to $\zeta = 1$ as a result of conduction outward from the water-filled shallow crevasse. After 30 years, scenario 4 produced temperate ice $10m$ in front of the fracture zone from $\zeta = 0.2$ to $\zeta = 0.5$. See Figure 5.7 for a 2D

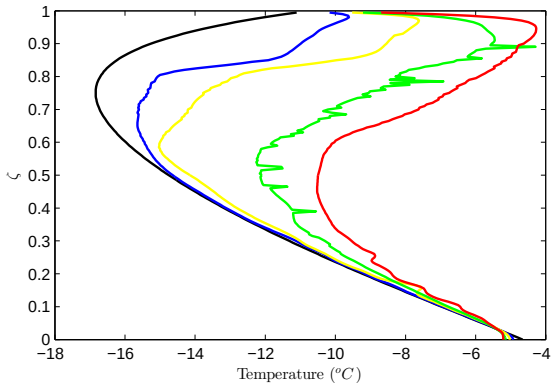

(a) Scenario 1, 25% retention, deep

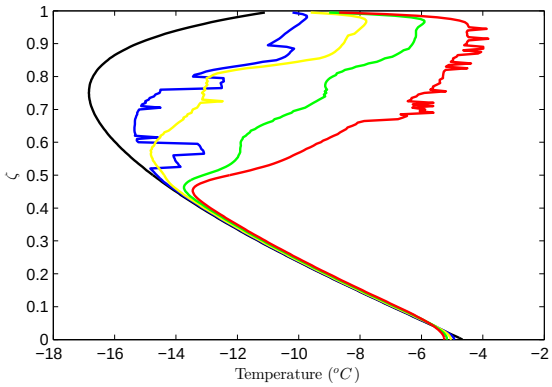

(b) Scenario 2, 25% retention, medium

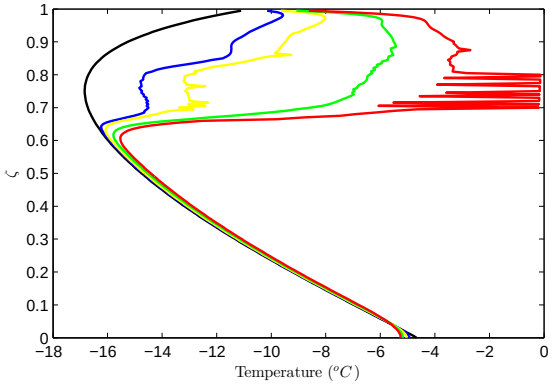

(c) Scenario 3, 25% retention, shallow

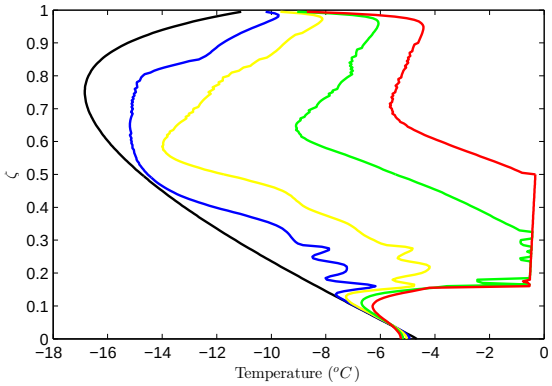

(d) Scenario 4, narrow (20m wide fracture zone)

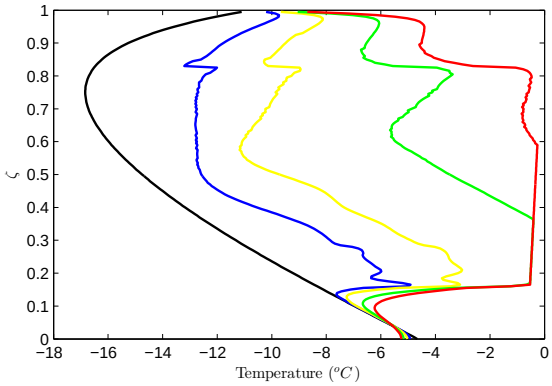

(e) Scenario 5, wide (50m wide fracture zone)

Figure 5.8: Vertical profiles 20m in front of crevasse. The black line is the initial temperature profile, blue is after 5 years of annual filling and draining, yellow is after 10 years, green is after 20 years, and red is after 30 years.

plot of warming after 40 years using filling and draining scenario 4.

Conversely, scenario 5 used a $50m$ wide fracture zone, so the vertical profiles shown fell within the fracture zone. While the same amount of enthalpy was distributed annually in scenarios 4 and 5, scenario 5 distributed it to a larger area, meaning the magnitude of warming was smaller, but more widespread. The vertical profiles shown fell within the fracture zone, however, so warming started immediately and temperature increased proportionally with time in the depths within the fracture zone. After 20 years, there was temperate ice from $\zeta = 0.2$ to $\zeta = 0.4$, and after 30 years the entire fracture zone was temperate or within 1^oC of θ_{PMP}.

Figure 5.9 shows depth-averaged temperatures at various distances in front of the crevasse over time using the five different fracturing models. Figure 5.9a shows the temperature over time resulting from fracturing scenario 1. We see the depth-averaged temperature of the entire ice sheet was initially -13^oC and the column 5m ahead of the crevasse experienced the greatest warming initially. There was roughly a 5 year delay before any warming was felt $40m$ ahead of the crevasse. At the columns closest to the crevasse, a distinct sinusoidal pattern is observed that results from the assumption that fracturing occurs in a single timestep. This caused a spike in the column temperature, which was followed by a decline. This decline occurred because liquid water was moved ahead of the crevasse during the fracturing event, but the horizontal velocity was slower at depth than at the depth of the crevasse. As a result, latent heat from the fractures at depth lagged behind the movement of the crevasse and cold ice from ahead of the crevasse moved into the columns shown in the figure. By 40 years, the depth-averaged temperature 5m ahead of the crevasse was warmed by 8^oC while the column 40m ahead of the crevasse was warmed by 6^oC. 8% of the nodes in the domain were temperate after 40 years, primarily in the immediate vicinity of the crevasse. While it may be surprising to see such great warming 40m ahead of the crevasse, it can be explained by the horizontal velocity gradient in the ice sheet. When a crevasse drained liquid water to depth in the ice sheet, its velocity was slower than the velocity of the crevasse. Over time, ice that was at one time under a crevasse ended up behind the crevasse. While a fracture rarely extended 40m in front of a crevasse, drained liquid water from the downstream crevasse in

a field would cause warming in a column 40m in front of the upstream crevasse.

Figures 5.9b and 5.9c show the depth-limited filling and draining cases. While scenario 2 shows a very similar depth-averaged warming pattern as scenario 1, scenario 3 shows that warming tapers in the columns closest to the crevasse at late time. After 20 years, the column $5m$ in front of the crevasse peaks at a temperature of roughly 8^oC. This is because the nodes in that column in the top $\frac{1}{3}$ of the ice sheet have become temperate, and the fracturing algorithm routes enthalpy to columns further ahead of the crevasse. The depth-averaged temperature stays cold, however, because only the top $\frac{1}{3}$ of the ice sheet experiences CHW and conduction downward provides little warming to the lower ice sheet in 40 years.

Figures 5.9d and 5.9e show depth-averaged warming for the cases with drainage into the characteristic rectangular area. In scenario 4 we see the distinct annual sinusoidal pattern at the column $5m$ ahead of the crevasse and in scenario 5 we see this pattern clearly in the columns 5m and 10m in front of the crevasse. These columns fell in their respective characteristic CHS, thus experiencing seasonal warming and cooling due to crevasse drainage. While in 5.9e we may expect the columns $5m$ and $10m$ to have the same temperature since the CHS extended $25m$ in front of the crevasse, the $5m$ column was slighly warmer because of conduction from the refreezing crevasse in the top of the ice sheet. By year 25, scenario 4 experienced a tapering of temperature in the column 5m in front of the crevasse and scenario 5 experienced this tapering both $5m$ and $10m$ in front of the crevasse. This was because the CHS in these scenarios became temperate and temperature below the CHS increased only slightly due to conduction after this time.

Figure 5.10 shows the increase in Glen's Flow Law Paramater A $20m$ in front of the crevasse after 40 years of filling and draining in the 5 scenarios. As expected, scenario 1 showed some increase in the Flow Law Paramter A at all depths while scenarios 2 and 3 only showed an increase above their depth thresholds. Scenario 3 showed a much greater increase than scenarios 1 and 2 above $\zeta = 0.66$ because all of the crevasse enthalpy was restricted to a smaller area. At its highest, scenario 3 experienced a 25 times increase in A at $\zeta = 0.8$. This depth of the ice sheet was coldest initially (see Figure 4.3), so had the greatest warming potential due to CHW. While scenario 5

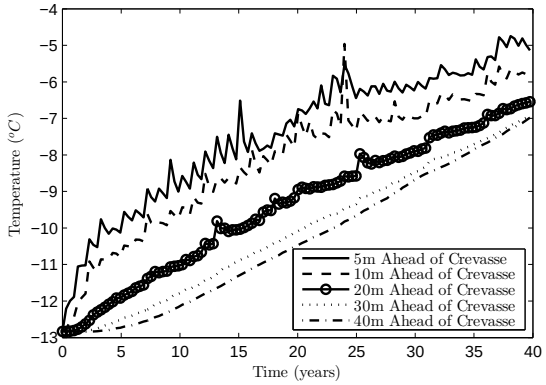

(a) Scenario 1, 25% retention, deep

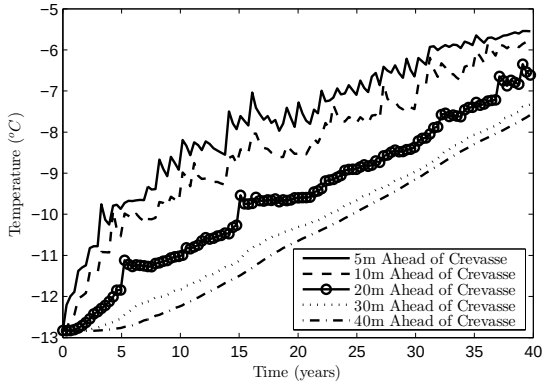

(b) Scenario 2, 25% retention, medium

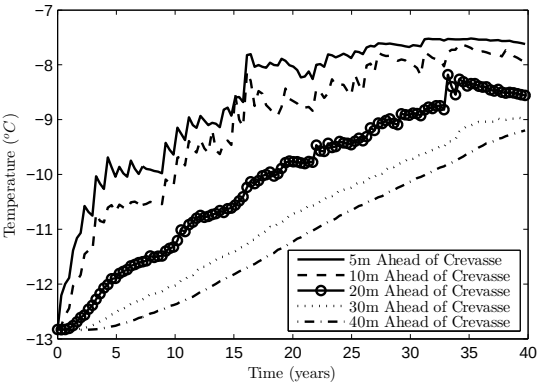

(c) Scenario 3, 25% retention, shallow

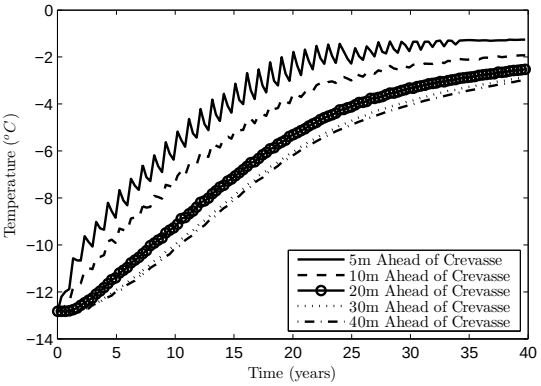

(d) Scenario 4, narrow

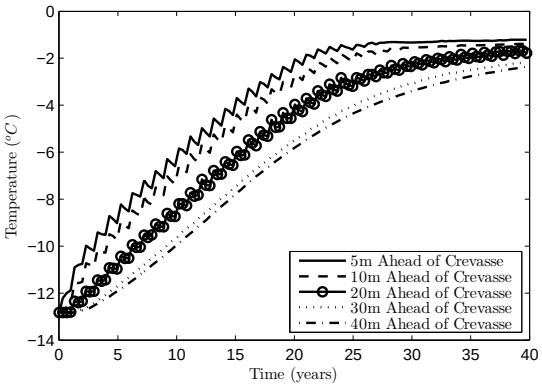

(e) Scenario 5, wide

Figure 5.9: Depth-averaged temperatures over time at varying locations in front of crevasse.

experienced the greatest increase of A (more than a 30 times increase), it experienced the same increase as scenario 4 below $\zeta = 0.6$. This was because below that depth, the higher horizontal velocity essentially "mixed" the annually added enthalpy so that the width of the rectangular CHS had no influence on the temperature after 40 years. In all 5 scenarios, only a small increase of A was observed at the bed $20m$ in front of the crevasse. At $\zeta = 0.1$, scenario 5 had the largest increase of 24% due to downward conduction from the overlying CHS. Scenario 1 experienced a 14% increase in A at $\zeta = 0.1$ due to the rare event of a water-filled fracture reaching that depth.

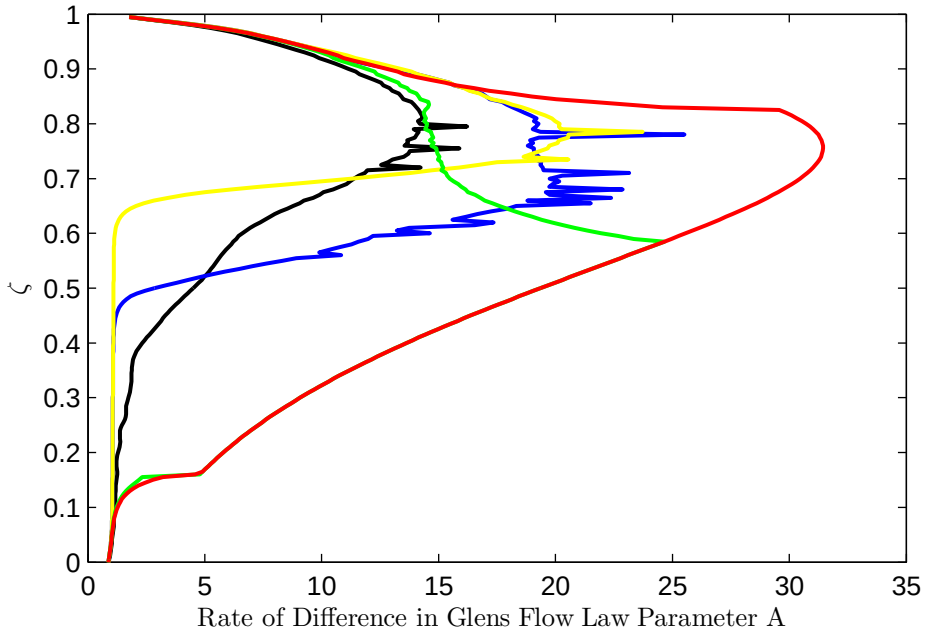

Figure 5.10: Increase in Glen's Flow Law Paramter A 20m in front of the crevasse. The black line is scenario 1, blue is scenario 2, yellow is scenario 3, green is scenario 4, and red is scenario 5.

Chapter 6

CHW Parameterizations

By nondimensionalizing the shallow crevasse refreezing problem using the crevasse width, crevasse spacing, and background ice temperature, we can derive 1D analytical solutions that approximate the horizontal conductive heating in front of and behind the crevasse. See Sections 6.1 and 6.2 for the derivation of these 1D analytical solutions. We can compare the warming in front of and behind the crevasse at shallow depth from our numerical model (Section 5.2) to the warming predicted by the Fourier Series analytical solution by assuming that the moving phase change interface at the crevasse wall, which the numerical solution captures, can be approximated by a stationary phase change interface. Also, the Fourier Series solution is only valid at times less than the refreezing time of the crevasse.

It is also possible to use a Laplace transformation method to find an approximate analytical solution of a refreezing moulin problem. See Section 6.3 for the solution and a comparison of refreezing time and warming from a crevasse and moulin.

As we see in Figure 5.3, there is good agreement between the numerical and Fourier Series solutions in front of the crevasse. The agreement between the numerical results and analytical solutions confirm that the warming resulting from a shallow crevasse can be well approximated by the assumption that heat is only conducted horizontally. This further suggests that any significant thermomechanical influence from CHW at depth in the ice sheet can only be accomplished by a delivery of liquid water at depth - not through vertical advection or vertical conduction.

After deriving these analytical solutions of warming for crevasses and moulins, we will discuss

their possible utility in CHW parameterizations for large-scale ice sheet models in section 6.4. We will also discuss the connection between these solutions and the existing CHW parameterization used in two Phillips et al. papers [34, 33]. Finally, we will discuss ideas for parameterizations that include the effect of diffuse fracture-based CHW (as discussed in section 5.4) in section 6.5.

6.1 Non-dimensional Fourier Series Crevasse Solution

One boundary condition at the crevasse half-width ($x = -W$) is held at $\theta = \theta_{PMP}$ while the other boundary condition is located at the crevasse half-spacing, $x = R$, and is a no-flux boundary condition. To obtain the 1D analytical solutions we can non-dimensionalize the thermal system by:

$$\xi = \frac{x}{R} \tag{6.1}$$

$$\tau = \frac{t\alpha_i}{R^2} \tag{6.2}$$

$$\Theta = \frac{\theta - \theta_0}{\theta_{PMP} - \theta_0} \tag{6.3}$$

and make the simplifying assumption that the crevasse / background ice interface remains fixed in space. With this assumption we can derive a Fourier Series solution:

$$\Theta(\xi, \tau) = 1 - 4\sum_{n=0}^{\infty} \frac{sin\left(\frac{(2n+1)}{2}\pi\xi\right)}{(2n+1)\pi} exp\left(-\frac{(2n+1)^2\pi^2}{4}\tau\right) \tag{6.4}$$

By applying a flux balance condition at the crevasse / background ice interface, we can derive the location of the crevase / background ice interface:

$$\xi_i(\tau) = -2\epsilon\sum_{n=0}^{\infty} \frac{4}{(2n+1)^2\pi^2}\left(1 - exp\left(\frac{-(2n+1)^2\pi^2}{4}\tau\right)\right) \tag{6.5}$$

where

$$\epsilon = \frac{\rho_i C_i}{\rho_w L}(\theta_{PMP} - \theta_0) \tag{6.6}$$

It is worth noting that at $\tau = \tau_f$, the refreezing time, the interface location is at $\xi_i = -\frac{W}{R}$. As $\tau \to \infty$:

$$\xi_i(\tau \to \infty) \to -2\epsilon\sum_{n=0}^{\infty} \frac{4}{(2n+1)^2\pi^2} = -\epsilon \tag{6.7}$$

which means that the crevasse / background ice interface can only move a distance $-\epsilon$ before the background ice becomes temperate. As seen in Figure 6.1, the Fourier Series Solution for $\sqrt{\tau_f}$ increases exponentially when $\frac{W}{R} \gtrsim 0.8\epsilon$ and asymptotes to $\tau_f \to \infty$ at $\frac{W}{R} = \epsilon$. This is because when $\frac{W}{R} \geq \epsilon$, there is sufficient enthalpy in the meltwater-filled crevasses that the background ice everywhere becomes temperate before all of the meltwater refreezes. Once this is the case, the ice and water are at the same temperature and no more refreezing takes place.

We can also see in Figure 6.1 that with the Fourier Series solution for large crevasse spacing (or $\frac{W}{R} \lesssim 0.8\epsilon$), the relationship between non-dimensional refreezing time, crevasse width, and creavsse spacing can be well approximated by:

$$\tau_f = \frac{\pi}{4\epsilon^2}\left(\frac{W}{R}\right)^2 \tag{6.8}$$

When re-dimensionalized, the relationship becomes:

$$t_f = \frac{\pi\left(\rho_w L\right)^2}{4\left(\rho_i C_i\left(T_m - T_0\right)\right)^2}\frac{W^2}{\kappa_i} \tag{6.9}$$

This is a key result indicating that with large crevasse spacing, warming and time to refreezing are a function of $\frac{W^2}{\kappa_i}$, not $\frac{R^2}{\kappa_i}$ as has been used in the parameterization scheme found in the two Phillips et al. papers [34, 33].

6.2 Non-dimensional Error Function Crevasse Solution

If we further assume that crevasse spacing is wide enough that the background ice can be treated as a semi-infinite domain, we can derive a simple Error Function solution for temperature:

$$\Theta\left(\xi, \tau\right) = erfc\left(\frac{\xi}{\sqrt{4\tau}}\right) \tag{6.10}$$

With the same assumptions, we can derive a solution for the refreezing time of a crevasse:

$$\tau_f = \frac{\pi}{4\epsilon^2}\left(\frac{W}{R}\right)^2 \tag{6.11}$$

As seen in Figure 6.1, the Error Function Solution for refreezing time agrees well with the Fourier Series Solution for small $\frac{W}{R}$ as refreezing takes place before the latent heat of refreezing reaches

the half-spacing boundary. When $\frac{W}{R} \gtrsim 0.8\epsilon$, the semi-infinite domain assumption no longer is valid and the Error Function solution underestimates the time for the crevasse to refreeze.

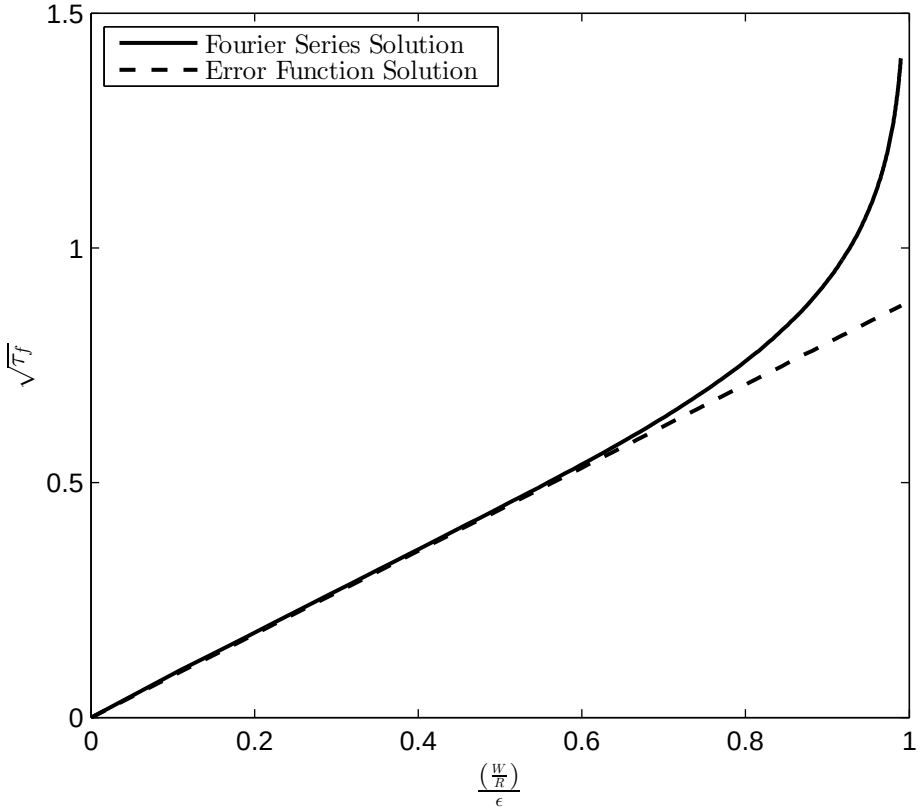

Figure 6.1: A comparison of the nondimensioanl solution of crevasse refreezing time resulting from two approximate analytical solutions. We see that the Error Function solution deviates from the Fourier Series solution for $\frac{W}{R} \gtrsim 0.8\epsilon$. In this regime, the Fourier Series solution is more accurate at capturing the thermodynamics of the system.

6.3 Radial Moulin Solution

Next, we examine the radial problem of a refreezing moulin of infinite length surrounded by an infinite domain of cold ice [7]. Conduction of heat in ice can be expressed radially as:

$$\frac{\partial \theta}{\partial t} - \frac{1}{r}\frac{\partial}{\partial r}\left(r\alpha_i \frac{\partial \theta}{\partial r}\right) = 0 \tag{6.12}$$

for $r > a$ where r is the radius from the moulin center, a is the initial moulin radius, and α_i is the ice diffusivity. Using a Laplace transformation, temperature in the cold ice can be described by:

$$\theta(r,t) = \theta_{PMP} + \frac{2(\theta_{PMP} - \theta_0)}{\pi} \int_0^\infty e^{-\alpha_i u^2 t} \frac{J_0(ur) Y_0(ua) - Y_0(ur) J_0(ua)}{J_0^2(au) + Y_0^2(au)} \frac{du}{u} \tag{6.13}$$

where θ_0 is the initial ice temperature, u is a dummy variable, J_0 is a Bessel function of the first type, and Y_0 is a Bessel function of the second type. Similarly, the flux at the moulin boundary is:

$$-\kappa_i \left.\frac{\partial \theta}{\partial r}\right|_{r=a} = \frac{4\kappa_i(\theta_{PMP} - \theta_0)}{\pi^2 a} \int_0^\infty e^{-K_i u^2 t} \frac{du}{u\left(J_0^2(au) + Y_0^2(au)\right)} \tag{6.14}$$

where κ_i is ice conductivity. At the moulin boundary, we use the flux condition:

$$-2\pi r \frac{dr}{dt} \rho_w L = -2\pi r \kappa_i \left.\frac{\partial \theta}{\partial r}\right|_{r=a} \tag{6.15}$$

where $\frac{dr}{dt}$ is the rate of moulin closure rate to derive:

$$\frac{d\left(\frac{r}{a}\right)}{d\tau_\infty} = \frac{-4(\theta_{PMP} - \theta_0)\rho_i C_i}{\pi^2 \rho_w L} \int_0^\infty e^{-\tau_\infty v^2} \frac{dv}{v\left(J_0^2(v) + Y_0^2(v)\right)} \tag{6.16}$$

where $\tau_\infty = \frac{\alpha_i t}{a^2}$ and v is a dummy variable.

Figure 6.2 shows that given the same width of a crevasse and diameter of a moulin, a moulin refreezes much faster. For the case of background ice at $-10^o C$, non-dimensional refreezing time can be found to be $\tau_{\infty f} = 31.5$ for a moulin and $\tau_{\infty f} = 197$ for a crevasse. Refreezing time can be found by re-dimensionalizing as $t_f = \frac{\tau_{\infty f} W^2}{\alpha_i}$ for a crevasse and $t_f = \frac{\tau_{\infty f} a^2}{\alpha_i}$ for a moulin. Figure 6.3 shows warming of background ice from the refreezing of a crevasse or moulin. Although a moulin refreezes faster, a crevasse of the same width warms the background ice to a greater extent because of its horizontal extent that is much larger than its width.

6.4 Parameterization for Shallow Crevasses

Figure 5.3 shows good agreement between our 2-dimensional numerical results (shown in non-dimensional form) and the analytical solution for warming derived in section 6.1. This confirms that the assumption that heat is only conducted horizontally from a crevasse is reasonable and can be used in a parameterization.

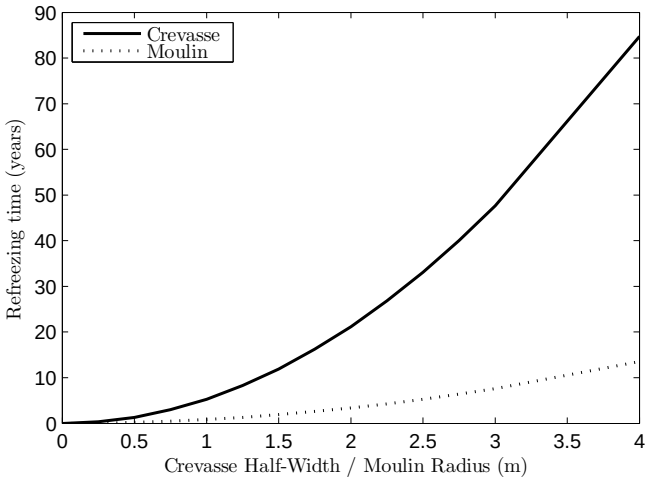

Figure 6.2: Refreezing time of a crevasse and moulin in background ice at -10^oC as a function of creavsse half-width or moulin radius.

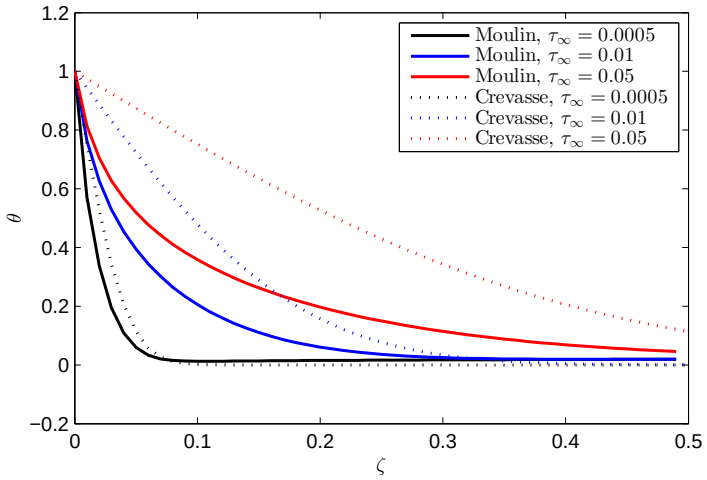

Figure 6.3: Warming of background ice initially at -10^oC produced by a crevasse with $1m$ half-width or a moulin with a $1m$ radius.

The ratio of crevasse width and crevasse spacing can be generalized as falling into three regimes. When $\frac{W}{R} \lesssim 0.8\epsilon$, the crevasse spacing is large enough that the crevasses are thermodynamically isolated and do not feel eachother's heat in the time it takes to refreeze. If $0.8\epsilon \lesssim \frac{W}{R} < \epsilon$, the crevasses are spaced close enough that refreezing is slowed as compared to an isolated crevasse case, but full refreezing does occur. When $\frac{W}{R} \geq \epsilon$, crevasses are spaced close enough that full refreezing never occurs and the background ice becomes temperate. These factors affect what

parameterization should be used.

For the large crevasse spacing case, we found in Section 6.1 that warming and time to refreezing are a function of $\frac{W^2}{\kappa_i}$, not $\frac{R^2}{\kappa_i}$ as has been used in the parameterization scheme found in Phillips et al. [34, 33]. The CHW linear exchange term parameterization found in equation 1.10 should perhaps be rewritten as:

$$\rho_i C_i \frac{\partial \theta_i}{\partial t} + \rho_i C_i u \frac{\partial \theta_i}{\partial x} + \rho_i C_i w \frac{\partial \theta_i}{\partial z} - \kappa_i \frac{\partial^2 \theta_i}{\partial z^2} = Q + \frac{\kappa_i}{W^2} \left(\theta_{CHS} - \theta_i\right) \tag{6.17}$$

and the winter CHW linear exchange term parameterization found in equation 1.11 would be rewritten as:

$$\frac{\partial \overline{\rho H}_{CHS}}{\partial t} - \frac{\partial}{\partial z} \left(\kappa_{CHS} \frac{\partial \theta_{CHS}}{\partial z} \right) = -\frac{k_i}{W^2} \left(\theta_{CHS} - \theta_{ice}\right) \tag{6.18}$$

For the close crevasse case with full refreezing, the crevasse spacing, or R, is still the dominant parameter affecting the linear exchange term between the CHS and average background ice temperature. Equations 1.10 and 1.11 seem to capture the correct physics of this situation, though the fact that the CHS equation (Equation 1.11) doesn't contain an advection term requires some thought. This is a problem for both the large crevasse spacing and small crevasse spacing parameterization. If we are allowing for the possibility of crevasses experiencing a one-time filling and then refreezing, it seems the CHS should advect with the background ice. If, however, we follow the scenario presented in Phillips et al. [34, 33], the CHS refills annually in the melt season and is allowed to partially or fully refreeze over the winter. If an alternative parameterization is used that includes advection of the CHS, Equation 1.11 would be written as:

$$\frac{\partial \overline{\rho H}_{CHS}}{\partial t} + \rho_i C_i u \frac{\partial \theta_{CHS}}{\partial x} - \frac{\partial}{\partial z} \left(\kappa_{CHS} \frac{\partial \theta_{CHS}}{\partial z} \right) = -\frac{k_i}{R^2} \left(\theta_{CHS} - \theta_{ice}\right) \tag{6.19}$$

Finally, for the very close crevasse spacing case, the background ice will become temperate even from a one-time filling. The amount of meltwater required to fill these crevasses would be immense, and although cases existed where the background ice was brought to $\theta_i = \theta_{PMP}$ in Phillips et al. [34, 33], this was only with a steady-state model that included annual fillings of the CHS with liquid water, not from a one-time filling. A parameterization when $\frac{W}{R} \geq \epsilon$ could be as

simple as bringing the ice to $\theta_i = \theta_{PMP}$, but would likely need to consider other more important factors involving the supraglacial hydrology.

6.5 Parameterization for Diffuse Fracture Networks

In the case that supraglacial meltwater is distributed into a diffuse fracture network, a different parameterization will be used than the shallow crevasse parameterization. As seen in Figure 5.6, fractures are narrow, refreeze quickly, and can cause uniform warming deep in the ice sheet as a result of high strain rates. Even with $100m$ spacing, warming is uniform horizontally below $\zeta = 0.4$. The amount of warming is a function of the volume of meltwater, the amount retained englacially (not run off or drained to the bed), the background ice temperature, and the spatial distribution vertically. We will assume that once liquid water is routed in fracutres and becomes stagnant, refreezing occurs quickly and can be approximated as instantaneous. Under these assumptions, a parameterization can simply employ an enthalpy balance that transfers the latent heat of fusion to a temperature increase. Equations 6.20 and 6.21 show such a parameterization.

$$\Delta\theta = \frac{\phi_w \rho_w \left(C_i \theta_{PMP} + L\right)}{\rho_i C_i} \tag{6.20}$$

$$\phi_w = \frac{V_w \ frac_{retained}}{V_i} \tag{6.21}$$

where V_w is the volume of liquid water in the unit cell initially (perhaps in a water filled crevasse or moulin), $frac_{retained}$ is the fraction of liquid water that remains stagnant in the diffuse CHS and is allowed to refreeze, and V_i is the volume of ice in the unit cell over which the parameterization is being applied. See Figures 4.1 and 4.6 for a schematic of a diffuse fracture network CHS in a unit cell. This parameterization would be applied under the entire horizontal extent of the CHS but only at the depths where high shear causes the fracture network to be stretched homogeneously. See Figure 6.4 for a schematic of where this high shear zone occurs.

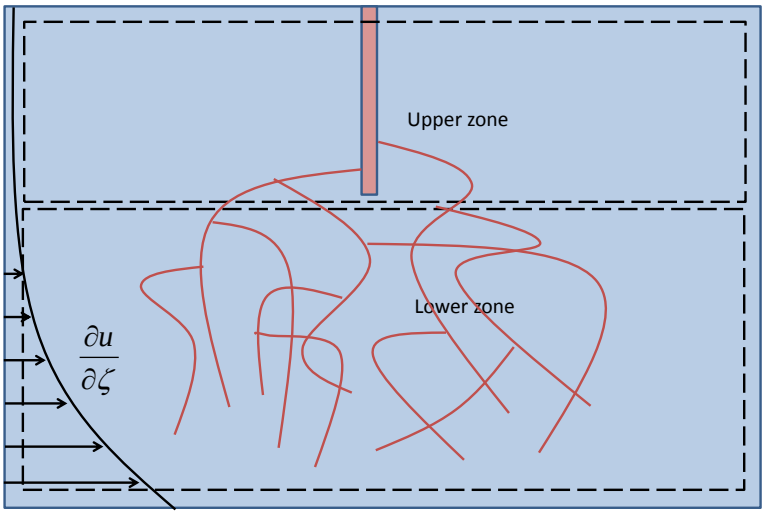

Figure 6.4: Schematic of a unit cell in the CHS domain parameterization that combines the discrete crevasse parameterization at shallow depths and the diffuse fracture network parameterization at depths with high shear in the ice sheet.

Chapter 7

GLIMMER-CISM Work

Another objective of my thesis was to develop a new Energy Equation solver for the Community Ice Sheet Model (CISM), the land ice component of the Community Earth System Model (CESM)[1] . CESM was created by the National Center for Atmospheric Research (NCAR) in 1983 and has grown over the past three decades to include users and developers from many Universities and National Laboratories. CESM is a fully-coupled, community, global climate model that provides state-of-the-art computer simulations of the Earth's past, present, and future climate states. It is one of the Global Climate Models (GCM) used in the Intergovernmental Panel on Climate Change (IPCC) reports to model past and future climate change scenarios. CISM is based on GLIMMER, an ice sheet model developed at the University of Bristol. CISM is a Fortran-95 based code that solves for ice sheet thickness and velocity with a Higher-Order solver. It is thermomechanically coupled and allows for a user-defined basal hydrology system. Presently, it only supports one-way coupling to CESM by using atmospheric data to force the surface boundary conditions of the ice sheet. The new Energy Equation solver is based on the approach outlined in [2]. The approach has been slightly modified to be compatible with the existing CISM framework (specifically boundary conditions and water drainage to the basal hydrologic network).

The main advantages to switching to an enthalpy formulation in CISM are a better ability to capture the basal temperate layer thickness, a more accurate estimate of drainage of liquid water to the subglacial hydrologic network, and a more accurate description for how the liquid water

[1] http://www2.cesm.ucar.edu/

fraction of temperate ice affects the ice rheology (through the Flow Law Rate Factor, A). As seen in Figure 7.1, the Flow Law Rate Factor A is dependent on ice temperature and water content [18]. Temperate ice that has a water fraction of 1% has a value for A that is 2.8 times higher than temperate ice with no water content. For a given value of applied stress, this larger rate factor will result in larger velocity gradients and thus larger velocities within the ice.

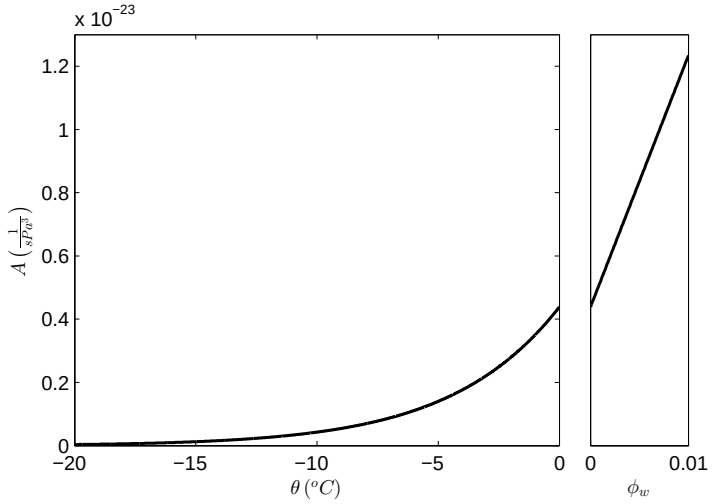

Figure 7.1: Flow Law Parameter A as a function of temperature and water fraction, ϕ_w

7.1 Current Temperature Solver

Currently a "cold ice" (i.e., ice with a temperature below that of the pressure melting point) solution is employed to solve the Energy Equation in CISM. Conservation of Energy is described by Equation 7.1:

$$\frac{\partial \theta}{\partial t} = \frac{k_i}{\rho_i C_i} \nabla^2 \theta - \mathbf{u} \cdot \nabla \theta + \frac{Q}{\rho_i C_i} \tag{7.1}$$

where θ is temperature, t is time, k_i is the thermal conductivity of ice, ρ_i is the density of ice, C_i is the heat capacity of ice, $\mathbf{u}$ is the ice velocity vector, and Q is strain heat. While this solution is exact for cold ice, polythermal conditions that include temperate ice require a simplification for the way liquid water is handled. In CISM, this is done by assuming that all liquid water generated internally immediately drains to the bed. In a timestep, this is done by setting temperatures above

the pressure-melting point to the pressure melting point and converting the excess sensible heat to liquid water, described by Equation 7.2:

$$melt = \frac{C_i H \left(\theta - \theta_{PMP}\right)}{\rho_i L \Delta\theta} \tag{7.2}$$

where melt is a length scale, H is the ice sheet thickness, θ_{PMP} is the pressure melting point, L is the latent heat of fusion, and $\Delta\theta = \theta - \theta_{PMP}$. In addition to the other shortcomings noted above, this method fails to accurately capture the location of the Cold-Temperate Surface (CTS) as it doesn't perform a flux balance across the CTS. This is especially problematic in the ablation zone where upward advection can cause an artificially large basal temperate layer to form.

7.2 Enthalpy-based Temperature and Water Fraction Solver

In this section, we will briefly lay out the approach from Aschwanden et al. [2] and describe how it was adapted for CISM. We can transform the Advection-Conduction Equation from a temperature-based equation into an Enthalpy-based equation by:

$$\overline{\rho H} = \left(1 - \phi_w\right) \rho_i C_i \left(\theta - \theta_0\right) + \phi_w \rho_w \left[C_i \left(\theta_{PMP} - \theta_0\right) + C_w \left(\theta - \theta_{PMP}\right) + L\right] \tag{7.3}$$

where $\overline{\rho H}$ is specific enthalpy, ϕ_w is internal liquid water fraction, and θ_0 is an arbitrary reference temperature. For cold ice and $\theta_0 = 0^o C$, this expression simply gives $\overline{\rho H} = \rho_i C_i \theta$. In this case, the Advection-Conduction equation (for cold ice and neglecting horizontal conduction, as is common in ice sheet models) is:

$$\frac{\partial \overline{\rho H}}{\partial t} + \mathbf{u} \cdot \nabla \overline{\rho H} - \frac{\partial}{\partial z}\left(\alpha \frac{\partial \overline{\rho H}}{\partial z}\right) = Q \tag{7.4}$$

where $\alpha = \frac{k}{\rho\, C}$ is the diffusivity of ice.

When dealing with temperate or polythermal conditions, a different formulation is needed for the conductive energy flux term. In cold ice, conductive flux is governed by Fourier's Law of Heat Transfer and is simply a sensible heat flux. In temperate ice, the conductive heat flux is the sum of a sensible and latent heat flux, which can both be expressed as diffusive processes. The sensible heat flux, $-k_i \nabla \theta_{PMP}$ arises from a temperature gradient due to spatial variations in

θ_{PMP}. Assuming hydrostatic conditions and the Clausius-Clapyron relation, however, means that θ_{PMP} varies linearly with depth, so $\frac{\partial \theta_{PMP}}{\partial z} = -\beta$, a constant. In a 1D column model, this results in $\frac{\partial}{\partial z}(-\beta) = 0$, so the sensible heat flux term can be neglected. In a 2D model, non-linear spatial variations in θ_{PMP} can exist in horizontally neighboring nodes with different ice depths, resulting in non-zero sensible heat exchange. Aschwanden et al.[2] showed that even with relatively steep surface slope, this term can reasonably be neglected. The latent heat flux results from diffusion of liquid water within temperate ice. The latent heat flux is proportional to the liquid water fraction, so can be expressed as $-k_0 \frac{\partial \phi_w}{\partial z}$, where k_0 is a small unknown diffusion-like parameter. Water fraction is now linearly related to enthalpy by:

$$\phi_w = \overline{\rho H} L^{-1} \tag{7.5}$$

when $\theta = \theta_{PMP}$. This allows us to define $\alpha_0 = \kappa_0 L^{-1}$ which is a small diffusivity and keep $\overline{\rho H}$ as our state variable. α_0 was chosen to be $\frac{\alpha_i}{100}$ to best match results from a 1D analytical solution of the Stefan problem for refreezing of liquid water (see Section 3.5). This diffusion of liquid water within ice is poorly understood, but has been observed to resemble a Fick-type diffusion. The conductive flux term for both cold and temperate ice is:

$$J_{conduction} = \begin{cases} -\alpha_i \frac{\partial \overline{\rho H}}{\partial z} & \overline{\rho H} < \overline{\rho H}_{PMP} \\ -k_i \frac{\partial T_{PMP}}{\partial z} - \alpha_0 \frac{\partial \overline{\rho H}}{\partial z} & \overline{\rho H} \geq \overline{\rho H}_{PMP} \end{cases} \tag{7.6}$$

where $\overline{\rho H}_{PMP}$ is the specific enthalpy of ice at $\theta = \theta_{PMP}$ with $\phi_w = 0$. We can now write out the full Advection-Conduction equation with the new conductive flux term:

$$\frac{\partial \overline{\rho H}}{\partial t} + \mathbf{u} \cdot \nabla \overline{\rho H} + \frac{\partial}{\partial z}(J_{conduction}) = Q \tag{7.7}$$

Once $\overline{\rho H}$ is calculated in each time-step, temperature and liquid water fraction can both be calculated as they are both functions only of enthalpy:

$$\theta = \begin{cases} \frac{\overline{\rho H}}{\rho_i C_i} & \overline{\rho H} < \overline{\rho H}_{PMP} \\ \theta_{PMP} & \overline{\rho H} \geq \overline{\rho H}_{PMP} \end{cases} \tag{7.8}$$

$$\phi_w = \begin{cases} 0 & \overline{\rho H} < \overline{\rho H}_{PMP} \\ \frac{\left(\overline{\rho H} - \overline{\rho H}_{PMP}\right)}{(\rho_w - \rho_i) C_i \theta_{PMP} \rho_w + L} & \overline{\rho H} \geq \overline{\rho H}_{PMP} \end{cases} \tag{7.9}$$

Temperature evolution in CISM is performed by operator splitting, meaning that the calculation of vertical conduction and strain heating are performed in one half timestep while vertical and horizontal advection are done in another half timestep. Since horizontal conduction is neglected, the conduction and strain heating solution is performed as a 1D solution for each column in the system. There are several dynamical cores (dycores) in CISM that perform temperature evolution and couple the solution thermomechanically in different manners. We concentrated on the **glissade** dycore that solves ice thickness and velocity with a higher-order solution and performs advection with an Incremental Remapping scheme. The new Enthalpy Gradient method is embedded in this existing dycore and can be switched on by changing the variable **whichtemp** to **TEMP_ENTHALPY**. Since the **temp** variable is pervasive in the dycore, we opted not to replace it with an enthalpy variable, but instead add a variable **waterfrac**, that along with **temp**, exactly describe the enthalpy of the system. Two subroutines, **enth2temp** and **temp2enth** are used to convert temperature and water fraction to specific enthalpy, and vice versa following the equations 7.3, 7.8, and 7.9. Before the conduction and strain heat half timestep, **temp** and **waterfrac** are converted to enthalpy, the solution for the current timestep is obtained, and enthalpy is converted back to **temp** and **waterfrac**. In the next half timestep, advection of **temp** and **waterfrac** is performed using the existing Incremental Remapping scheme, which is equivalent to advecting enthalpy.

7.3 Enthalpy-based Drainage Model

As temperatures above the pressure-melting point are encountered, liquid water is produced englacially. With the current temperature solver, any excess energy is converted to liquid water and immediately drained to the bed. With the Enthalpy Method, the ice matrix can support a liquid water fraction, ϕ_w. In Pettersson et al. [32] it is observed that above some threshold value drainage of this liquid water fraction occurs. In CISM, a maximum water fraction of $\phi_{w,max} = 0.01$ is used.

Although a basal temperate layer is most common, a surface temperate layer is also possible (see Figure 7.2). When $\phi_w > \phi_{w,max}$, the excess liquid is drained downward. In the basal temperate layer case, the liquid water enters the subglacial hydrology system as defined by **glissade**. In the surface temperate layer case, the liquid water drains to the underlying cold layer and is allowed to diffuse with diffusivity α_0. The refreezing of this liquid water and release of latent heat provides a source of warming to the cold ice layer.

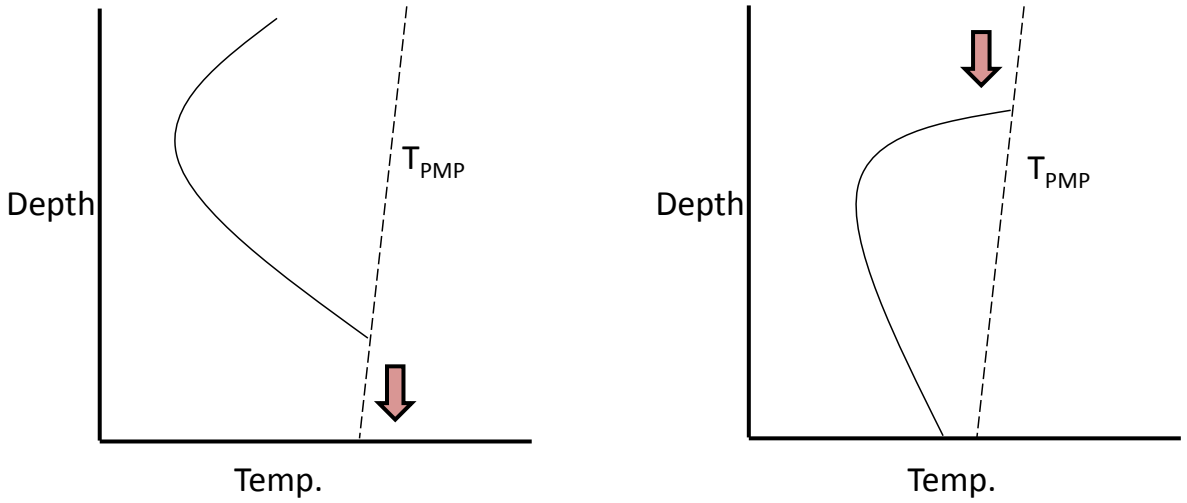

Figure 7.2: Left: a basal temperate layer that experiences drainage to the bed when $\phi_w > \phi_{w,max}$. Right: a surface temperate layer that experiences drainage to the cold layer below it. In both figures, the red arrow represents movement of liquid water downward by a preferential pathway mechanism that can be treated as a Fick-type diffusion.

7.4 Validation of Enthalpy Formulation

After implementing the Enthalpy-based approach, a validation of the new approach and comparison against the temperature-based approach were required. Since much of the model functions as a black box (as far as we are concerned), and segregating the thermal calculation is intractable, validation is difficult. Two tests can be performed to validate the new Enthalpy approach easily: One is to compare the temperature-based model and enthalpy-based model in cold conditions where

the two formulations should produce identical temperatures. The second is to do an energy balance on the enthalpy-based model in a single timestep in a node of the domain that is temperate to make sure the liquid water fraction is valid. There is no equivalent result from the temperature-based model to compare to since it did not calculate a liquid water fraction.

To validate the model, the Dome test case was used, which models a parabolic dome of ice with a floating margin. The dynamics of the problem dictate that as the ice flows from the summit outward, warming is produced from strain heat. It was first run with the old temperature-based physics, with **whichtemp** set to **PROGNOSTIC**. Next, it was run with the new enthalpy-based formulation, with **whichtemp** set to **TEMP_ENTHALPY**. In both cases, the test case was run for 200 years with 1 year timesteps. The domain had 10 thickness layers and had an area of 31 x 31 nodes on a $2000m$ x $2000m$ grid. The **glam** dycore was used, which is required for the enthalpy formulation, but is optional for the temperature-based formulation. A no-slip basal boundary condition was used and the ice was initially -15^oC everywhere. The built-in SLAP linear solver and JFNK non-linear solvers were used.

The first validation involves running the Dome test case at a time when the entire domain remains cold. Figure 7.3 shows a comparison between the temperature-based model and enthalpy-based model at $time = 50\ years$ and $\zeta = 0.94$. Manual examination of the results show that the entire domain is cold. From visual examination of the data, we see that the two formulations produce identical temperatures. Figure 7.4 shows the warming of one particular node from $time = 0\ years$ to $time = 50\ years$ using both formulations. Again, we see that this particular node warms at exactly the same rate as it and all of its neighboring nodes remain cold. These results indicate that, as expected, the new enthalpy formulation is identical to the old temperature-based formulation when and where the domain is cold.

The next validation problem to consider is when temperate ice is encountered. As the temperature-based formulation drains all melt water immediatly to the bed, there is no way to validate our new formulation against the original formulation. Figure 7.5 shows the layer of the dome at $\zeta = 0.94$ after 200 years with the new enthalpy-based formulation. As we can see from the

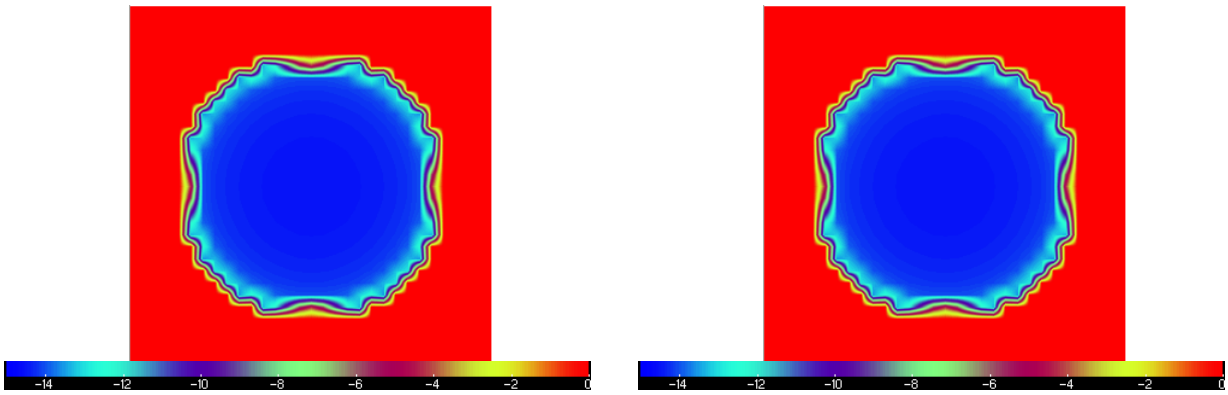

(a) Temperature at $\zeta = 0.94$ with temperature-based model

(b) Temperature at $\zeta = 0.94$ with enthalpy-based model

Figure 7.3: Comparison of Temperature and Enthalpy-based dome problem at $t = 50$ $years$. The domain is cold at all nodes.

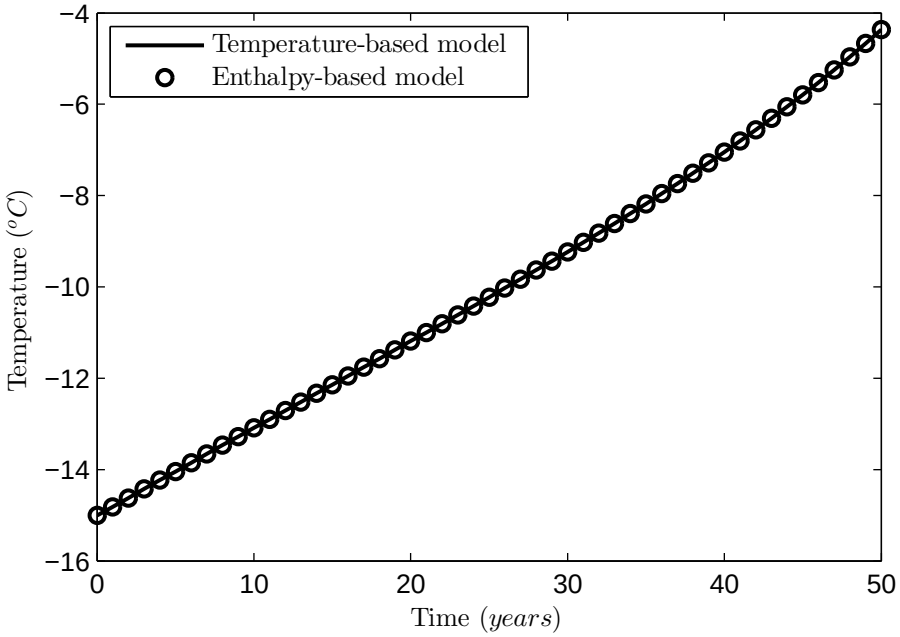

Figure 7.4: Temperature increase over 50 years in a cold node of the dome problem. The node is located at $x = 50000m$, $y = 30000m$, $\zeta = 0.94$.

plots of temperature and water fraction, temperate ice is encountered at the margins of the domain. We can see that strain heat dissipation is highest in these same nodes, explaining why they are the first to become temperate. The Flow Law Parameter A is a function of water fraction with the new formulation. It is highest in the temperate nodes, causing a positive feedback mechanism whereby the velocity becomes higher because of the Flow Law Parameter A, and strain heat from the higher velocities causes a rise in the liquid water fraction.

We can now perform an energy balance at one particular temperate node during one timestep. At $\zeta = 0.888$, $x = 50000m$, $y = 32000m$ and $t = 100$ $years$, dissipation dimensionalized as temperature $\left(\frac{Q}{\rho_i C_i}\right) = 0.9925 \frac{^oC}{year}$. As this node is temperate at $t = 100$ $years$ if we assume that the increase in liquid water fraction is due only to strain heat dissipation, we can approximately validate that our changes to CISM result in the correct increase in liquid water fraction. It should be noted that strain heat dissipation is calculated independently of our new enthalpy-based formulation and no changes have been made to this part of the model. This is not a perfect assumption as the

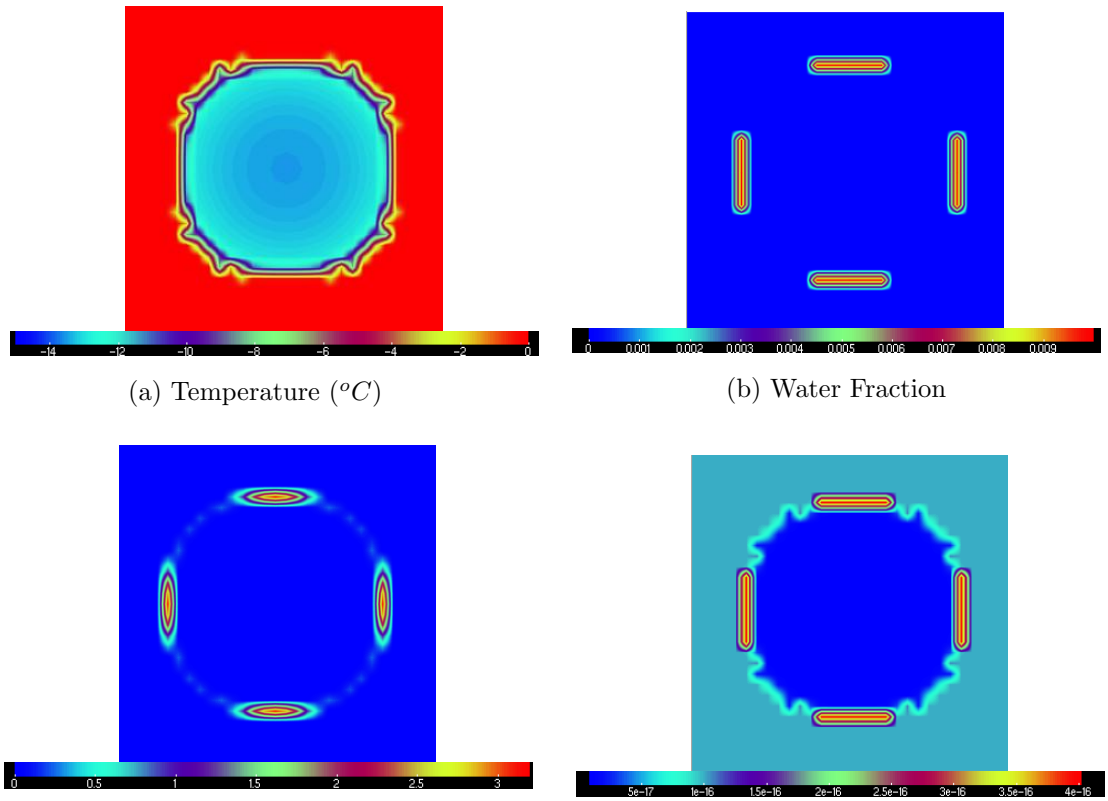

(a) Temperature (^oC)

(b) Water Fraction

(c) Dissipation $\frac{Q}{\rho_i C_i}$ $\left(\frac{K}{year}\right)$

(d) Flow Law Parameter A $\left(\frac{1}{sPa^3}\right)$

Figure 7.5: Dome problem with enthalpy-based model at $\zeta = 0.94$ and $time = 200$ $years$

physics of our enthalpy formulation dictates that there will be an advective flux of enthalpy and a small non-advective diffusion of liquid water. Equations 7.10 and 7.11 show the predicted increase in liquid water fraction as a result of strain heat during this timestep.

$$Q = 0.9925 \frac{^oC}{year} * \rho_i * C_i = 1814620 \frac{J}{m^3\ year} \tag{7.10}$$

$$\Delta\phi_w = \frac{\Delta\left(\overline{\rho H} - \overline{\rho H}_{PMP}\right)}{\left(\rho_w - \rho_i\right) C_i \theta_{PMP} + \rho_w L} = \frac{1814620 \frac{J}{m^3 year}}{334957381 \frac{J}{m^3 year}} = 0.0054 \tag{7.11}$$

This says that we would expect the liquid water fraction in this node to increase by 0.54% from $time = 100\ years$ to $time = 101\ years$ if there were no advection, non-advective flux of liquid water, or drainage of liquid water. We actually see that $\left(\phi_w\left(t = 101\ years\right) - \phi_w\left(t = 100\ years\right)\right) = 0.0048$, which is slightly lower than calculated. The difference is small, however, and can be explained by advection and diffusion of enthalpy to neighboring nodes, especially since our chosen node has a locally high liquid water fraction at $t = 100\ years$.

Bibliography

[1] Richard B. Alley, Todd K. Dupont, Bryon R. Parizek, and Sridhar Anandakrishnan. Access of surface meltwater to beds of sub-freezing glaciers: preliminary insights. Annals of Glaciology, 40:8–14, 2005.

[2] Andy Aschwanden, Ed Bueler, Constantine Khroulev, and Heinz Blatter. An enthalpy formulation for glaciers and ice sheets. Journal of Glaciology, 58(209):441–457, 2012.

[3] H. Bader and F. Small. Sewage disposal at ice cap installations. Technical Report 21, Snow Ice Permafrost Research Establishment, 1955.

[4] Sarah Boon and Martin Sharp. The role of hydrologically-driven ice fracture in drainage system evolution in an Arctic glacier. Geophysical Research Letters, 30(18), 2003.

[5] J. E. Box, X. Fettweis, J. C. Stroeve, M. Tedesco, D. K. Hall, and K. Steffen. Greenland ice sheet albedo feedback: thermodynamics and atmospheric drivers. The Cryosphere, 6:821–839, 2012.

[6] W. F. Budd. The dynamics of ice masses. Antarct. Div., Dep. of Supply 108, ANARE Sci. Rep. Publ., Melbourne, Victoria, Australia, 1969.

[7] H. S. Carslaw and J. C. Jaeger. Conduction of Heat in Solids. Oxford Science Publications, second edition, 1946.

[8] G. A. Catania and T. A. Neumann. Persistent englacial drainage features in the Greenland ice sheet. Geophysical Research Letters, 37(2), 2010.

[9] Ginny A. Catania, Thomas A. Neumann, and Stephen F. Price. Characterizing englacial drainage in the ablation zone of the Greenland ice sheet. Journal of Glaciology, 54(187), 2008.

[10] Garry K. C. Clarke and Gary T. Jarvis. Post-surge temperatures in Steele Glacier, Yukon Territory, Canada. Journal of Glaciology, 16(74):261–268, 1976.

[11] Caroline Clason, Douglas W. F. Mair, David O. Burgess, and Peter W. Nienow. Modelling the delivery of supraglacial meltwater to the ice/bed interface: application to southwest Devon Ice Cap, Nunavut, Canada. Journal of Glaciology, 58(208):361–374, 2012.

[12] W. Colgan, K. Steffen, W. S. McLamb, W. Abdalati, H. Rajaram, R. Motyka, T. Phillips, and R. Anderson. An increase in crevasse extent, West Greenland: Hydrologic implications. Geophysical Research Letters, 38(18), 2011.

[13] K. M. Cuffey and W. S. B. Paterson. The Physics of Glaciers. Elsevier, fourth edition, 2010.

[14] Janneke Ettema, Michiel R. van den Broeke, Erik van Meijgaard, Willem Jan van de Berg, Jonathan L. Bamber, Jason E. Box, and Roger C. Bales. Higher surface mass balance of the Greenland ice sheet revealed by high-resolution climate modeling. Geophysical Research Letters, 36(12), 2009.

[15] Andrew G. Fountain, Robert B. Schlichting, Peter Jansson, and Robert W. Jacobel. Observations of englacial water passages: a fracture-dominated system. Annals of Glaciology, 40:25–30, 2005.

[16] A. C. Fowler. On the transport of moisture in polythermal glaciers. Geophys. Astrophys. Fluid Dynamics, 28(2):99–140, 1984.

[17] Wouter Greuell. Melt-water accumulation on the surface of the Greenland ice sheet: Effect on albedo and mass balance. Geografiska Annaler: Series A, Physical Geography, 82(4):489–498, 2000.

[18] Ralf Greve and Heinz Blatter. Dynamics of Ice Sheets and Glaciers. Springer, Berlin, first edition, 2009.

[19] Edward Hanna, Philippe Huybrechts, John Cappelen, Konrad Steffen, Roger C. Bales, Evan Burgess, Joseph R. McConnell, Joergen Peder Steffensen, Michiel Van den Broeke, Leanne Wake, Grant Bigg, Mike Griffiths, and Deniz Savas. Greenland ice sheet surface mass balance 1870 to 2010 based on twentieth century reanalysis, and links with global climate forcing. Journal of Geophysical Research: Atmospheres (19842012), 27(D24), 2011.

[20] Edward Hanna, Philippe Huybrechts, Konrad Steffen, John Cappelen, Russell Huff, Christopher Shuman, Tristran Irvine-Fynn, Stephen Wise, and Michael Griffiths. Increased runoff from melt from the Greenland ice sheet: A response to global warming. Journal of Climate, 21:331–341, 2008.

[21] J. Harper, N. Humphrey, W. Tad Pfeffer, J. Brown, and X. Fettweis. Greenland ice-sheet contribution to sea-level rise buffered by meltwater storage in firn. Nature, 491(7423):240–243, 2012.

[22] P. Holmlund. Internal geometry and evolution of mouline, Storglaciaren, Sweden. Journal of Glaciology, 34:242–248, 1988.

[23] Roger Leb. Hooke. Principles of Glacier Mechanics. Cambridge University Press, second edition, 2005.

[24] N. F. Humphrey, J. T. Harpher, and W. Tad Pfeffer. Thermal tracking of meltwater retention in Greenland's accumulation area. Journal of Geophysical Research-Earth Surface, 117(F1), 2012.

[25] K. Hutter. A mathematical model of polythermal glaciers and ice sheets. Geophys. Astrophys. Fluid Dynamics, 21:201–224, 1982.

[26] Gary T. Jarvis and Garry K. C. Clarke. Thermal effects of crevassing on Steele Glacier, Yukon Territory, Canada. Journal of Glaciology, 13(68):243–254, 1974.

[27] Ian Joughin, Sarah B. Das, Matt A. King, Ben E. Smith, Ian M. Howat, and Twila Moon. Seasonal speedup along the Western flank of the Greenland ice sheet. Science, 320(5877):781–783, 2008.

[28] Virgil J. Lunardini. Heat Transfer in Cold Climates. Van Nostrand Reinhold Co., New York, New York, first edition, 1981.

[29] Daniel McGrath, William Colgan, Nicolas Bayou, Atsuhiro Muto, and Konrad Steffen. Recent warming at Summit, Greenland: Global context and implications. Geophysical Research Letters, 40(10):2091–2096, 2013.

[30] Daniel McGrath, William Colgan, Konrad Steffen, Phillip Lauffenburger, and James Balog. Assessing the summer water budget of a moulin basin in the Sermeq Avannarleq ablation region, Greenland ice sheet. Journal of Glaciology, 57(205):954–964, 2011.

[31] Thomas L. Mote. Greenland surface melt trends 19732007: Evidence of a large increase in 2007. Geophysical Research Letters, 34(22), 2007.

[32] R. Pettersson, P. Jansson, and H. Blatter. Spatial variability in water content at the cold-temperate transition surface of the polythermal Storglaciaren Sweden. Journal of Geophysical Research, 109, 2004.

[33] Thomas Phillips, Harihar Rajaram, William Colgan, Konrad Steffen, and Waleed Abdalati. Evaluation of cryo-hydrologic warming as an explanation for increased ice velocities in the wet snow zone, Sermeq Avannarleq, West Greenland. Journal of Geophysical Research: Earth Surface, 118:1–16, 2013.

[34] Thomas Phillips, Harihar Rajaram, and Konrad Steffen. Cryo-hydrologic warming: A potential mechanism for rapid thermal response of ice sheets. Geophysical Research Letters, 37, 2010.

[35] A. K. Rennermalm, L. C. Smith, V. W. Chu, J. E. Box, R. R. Forster, and M. van den Broeke. Evidence of meltwater retention within the Greenland ice sheet. The Cryosphere Discussions, 6(4):3369–3396, 2012.

[36] U. Spring and K. Hutter. Conduit flow of a fluid through its solid phase and its application to intraglacial channel flow. International Journal of Engineering Science, 20(2), 1982.

[37] T. Stenborg. Studies of the internal drainage of glaciers. Geografiska Annaler, 51A(1-2), 1969.

[38] M. Tedesco, X. Fettweis, T. Mote, J. Wahr, P. Alexander, J. Box, and B. Wouters. Evidence and analysis of 2012 Greenland records from spaceborne observations, a regional climate model and reanalysis data. The Cryosphere, 7:615–630, 2013.

[39] H. Thomsen and L. Thorning. Ice temperature profiles for West Greenland. Technical Report 92, Groenlands Geologiske Undersoegelse, 1992.

[40] C. J. van der Veen. Fracture propagation as means of rapidly transferring surface meltwater to the base of glaciers. Geophysical Research Letters, 34(1), 2007.

[41] J. Weertman. Can a water-filled crevasse reach the bottom surface of a glacier? Union Géodésique et Géophysique Internationale. Association Internationale d'Hydrologie Scientifique. Commission de Neiges et Glaces. Symposium on the Hydrology of Glaciers, 95:139–145, 1973.

[42] Stephen Whitaker. The Method of Volume Averaging. Kluwer Academic Publishers, Dordrecht, The Netherlands, 1999.